

Dephasing in binary black hole mergers surrounded by scalar wave dark matter clouds

Cheng-Hsin Cheng,^{1,*} Giuseppe Ficarra,^{2,†} and Helvi Witek^{1,3,‡}

¹*The Grainger College of Engineering, Department of Physics and Illinois Center for Advanced Studies of the Universe, University of Illinois Urbana-Champaign, Urbana, Illinois 61801, USA*

²*Dipartimento di Fisica, Università della Calabria, Arcavacata di Rende (CS), 87036, IT*

³*Center for AstroPhysical Surveys, National Center for Supercomputing Applications, University of Illinois Urbana-Champaign, Urbana, IL, 61801, USA*

(Dated: October 24, 2025)

Scalar fields of masses between 10^{-21} and $10^{-11}\text{eV}/c^2$ can exhibit enhanced gravitational interactions with black holes, and form scalar clouds around them. Such a cloud modifies the dynamics of a coalescing black-hole binary, and the resulting gravitational waves may provide a new channel to detect light scalar fields, such as axion-like particles or wave-like dark matter candidates. In this work we simulate a series of black-hole mergers with mass ratios $q = 1$ and $q = 1/2$, immersed in an scalar field overdensity with masses in the range $M\mu_S \in [0, 1.0]$. To do so, we implemented a constraint-satisfying initial data solver based on the puncture method, we improved the accuracy of our open-source software CANUDA to eighth order finite differences, and we reduced the initial orbital eccentricity. We investigate the impact of the scalar mass on the gravitational and scalar radiation. We find that binaries can undergo a delayed or an accelerated merger with respect to the vacuum. Our study highlights the challenge and importance of accurately modeling black-hole binaries in dark matter environments.

CONTENTS

I. Introduction	1
II. General relativity and massive scalars	3
A. Action and equations of motion	3
B. Time evolution formulation	3
C. Gravitational wave extraction	4
III. Initial data for black-hole binaries immersed in a scalar cloud	5
A. Constraints with scalar field contributions	5
B. Well-posedness of the Hamiltonian constraint	6
C. Initial scalar field profile	7
IV. Numerical relativity framework	7
A. Software description	7
B. Initial data solver: TwoPUNCTURES_BBHSF	8
C. Simulation setup	9
V. Results	10
A. Evolution of the binary-cloud system	10
B. Evolution of black hole properties	12
C. Scalar radiation	13
D. Gravitational radiation	14
E. Trends of physical observables	16
VI. Conclusions	18

VII. Acknowledgements

19

A. BSSN formulation of the Einstein–Klein-Gordon equations	19
B. Convergence test and error estimate	20
References	23

I. INTRODUCTION

In 2015, the direct detection of a gravitational wave (GW) signal emitted from a black hole (BH) binary coalescence [1] by the LIGO/Virgo Collaboration marked the dawn of GW astronomy, and paved the way for a new era of breakthroughs in fundamental physics. To this day, over 300 direct GW detections have been confirmed [2]. GW observations provide an exquisite window to gather insights on the properties of astrophysical BHs and their surrounding environments. Upcoming ground-based GW detectors such as the Einstein Telescope [3] or Cosmic Explorer [4], and space-based missions such as LISA [5], will enable us to infer properties about these BH binaries and their environments with even higher sensitivity.

One of the most tantalizing prospects of probing fundamental physics through GWs is that of shedding light on the nature of dark matter, a key open problem in modern physics. In recent years, scalar fields with masses below the eV scale arose as compelling dark matter candidates, given their influence on the growth of cosmic structure [6]. Excitingly, BHs can be used as probes for massive scalar fields when the (reduced) Compton wavelength of the scalar is comparable to the gravitational radius of the BH. This condition is commonly expressed in terms

* chcheng3@illinois.edu

† giuseppe.ficarra@unical.it

‡ hwitek@illinois.edu

of the product of BH and scalar masses as [7, 8]

$$\frac{GM_{\text{BH}}}{c^2} \left[\frac{\hbar}{m_S c} \right]^{-1} \sim 10^{10} \left[\frac{M_{\text{BH}}}{M_\odot} \right] \left[\frac{m_S}{\text{eV}/c^2} \right] \sim \mathcal{O}(1), \quad (1)$$

where M_{BH} is the BH's mass and $m_S = \hbar\mu_S$ is the scalar's physical mass. For astrophysical BHs ranging from stellar-mass to supermassive ones, $5 \lesssim M_{\text{BH}}/M_\odot \lesssim 10^{10}$, the criterion in Eq. (1) implies that BHs can be sensitive probes of ultralight scalars with masses between 10^{-21} eV and 10^{-11} eV. This range encompasses axion-like particles as well as fuzzy dark matter candidates.

The average density of galactic dark matter is very low with $\rho_{\text{DM}} \sim 0.01 M_\odot/\text{pc}^3$ [9]. For the effects of dark matter to have a sizable impact on the dynamics of astrophysical BHs, the density of dark matter has to be enhanced, which can be achieved if a portion of dark matter consists of massive scalar fields. Field overdensities up to $10^{18} M_\odot/\text{pc}^3$ can arise from the adiabatic growth of dark matter minispikes [10–15], up to $10^8 M_\odot/\text{pc}^3$ from accretion in a solitonic core [16, 17], depending on the cloud's angular momentum as well as parameters describing the BH [18, 19]. Another example of such an enhancement process is the superradiant instability, where a massive bosonic field extracts energy and angular momentum from a rotating BH, favoring the macroscopic growth of a bosonic cloud in its surroundings [7, 20–25], potentially yielding synchronised BH hair [26, 27]. Such (quasi-)stationary bosonic clouds can grow up to a few percent of the BH mass [20, 24], with densities reaching 10^{-5} in geometric units, corresponding to $10^{23} M_\odot/\text{pc}^3$ for a BH of mass $10^6 M_\odot$. As the superradiant cloud grows and the BH spins down, the depletion of BH populations in the superradiant region of the BH mass-spin plane can provide indirect evidence for BH superradiance or exclude fields of a given mass parameter [28–30].

In the presence of a sufficiently large scalar field overdensity, the dynamics of a BH binary can be altered, potentially leading to observable signatures in their gravitational waveforms [31–35]. Therefore, when modeling such GW sources, a non-negligible environment will need to be carefully considered [36–40]. With the scalar field accreted onto individual BHs [16, 18], the overdensities act as orbiting scalar “charges” which radiate energy from the system [41]. The formation of a scalar “wake” trailing the BHs has also been investigated numerically and analytically, which results in a dynamical friction force dragging the BHs as they move through the medium [42–45]. Additional features are also expected to arise due to tidal deformations, where the scalar clouds may be depleted in some circumstances [46–48]. Moreover, the presence of self-gravitating field configurations, such as dark matter cores and boson stars, can further affect the dynamics of inspiraling BH binaries [49–51].

If the GW source is an extreme mass-ratio inspiral (EMRI), where a primary, supermassive BH is perturbed by a secondary, stellar-mass BH, the scalar field overdensity is expected to persist around the secondary BH during the EMRI evolution [52–57]. Recent developments

using perturbation theory have enabled the calculation of fully-relativistic waveform templates for EMRIs in a scalar field environment [58–60]. In EMRIs as well as intermediate mass-ratio inspirals, the presence of a dark matter environment can be detectable by future GW observations [61], significantly enhance the merger event rate [62], and cause dephasing in the GW signal from energy dissipation due to dynamical friction [13, 15].

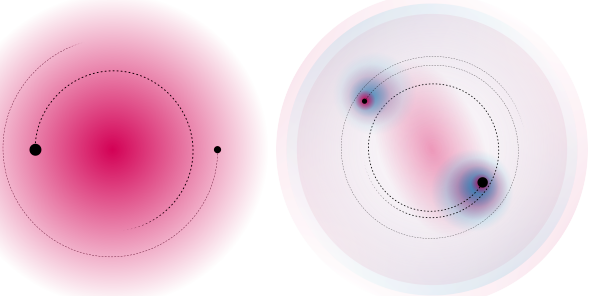


FIG. 1. Sketch of an unequal-mass BH binary interacting with a massive scalar cloud. Solid black circles indicating the BHs, their trajectories as dotted and dashed lines, and the oscillating scalar field represented by color. Left panel: Initial configuration of the binary and scalar cloud that is set up as spherically symmetric Gaussian profile at the BHs' center-of-mass. Right panel: The system one orbit into the inspiral. Around the BHs, the scalar field forms a pair of scalar overdensities that generate scalar radiation.

In this paper, we focus on the impact of a scalar cloud on comparable-mass BH binaries, as illustrated in Fig. 1. For the early inspiral, earlier works have characterized modifications to the GW signals [34, 63–65]. On the other hand, the nonlinear regime that unfolds during the merger is less well-understood, and a consistent solution of both the initial data and the evolution of the Einstein–Klein-Gordon equations is needed. Taking into account the scalar cloud back-reaction in the evolution alone, simulations have shown that the presence of the massive scalar cloud can affect the GW ringdown [66]. Recently, the construction of constraint-satisfying initial data has been made possible by a modification of the conformal transverse-traceless formalism called the “CTTK” method [67], which has been used to show that a scalar environment can lead to strong dephasing of the GW signal [68, 69]. A similar approach helped identify kicks in simulations of spinning and unequal-mass binaries evolved for a few orbits before merger [70].

In the present work, we adopt the puncture method for conformally flat BH binaries [71], and prescribe the profile the (conformally rescaled) scalar field itself. With massive scalar field back-reaction in the initial data, evolution, and waveform extraction, the primary goal of this work is to explore the impact of the scalar field mass on the gravitational waveform. We consider equal-mass and unequal-mass BH binaries with mass ratios $q = 1$ and $q = 1/2$, respectively. We vary the scalar's mass parameter in the range $M\mu_S \in [0.0, 1.0]$. Our simulations found

that quasi-circular binaries can undergo an accelerated or a delayed merger, depending on the scalar's and BHs' properties. Moving beyond proof-of-principle simulations of quasi-circular inspirals, we make several improvements to our software to produce gravitational waveforms that are suitable for template building and parameter estimation studies. In particular, we have implemented a new, constraint-satisfying initial data solver TwoPUNCTURES_BBHSF [72], that is publicly available in the EINSTEIN TOOLKIT [73–75]. We performed careful eccentricity reduction to ensure that the binary is quasi-circular with a sufficiently small eccentricity comparable to that used for GW analysis of vacuum BH binaries. We upgraded our open-source software CANUDA [76], to provide up to eighth order finite differences in the spacetime and scalar evolution, and in the wave extraction. With the enhanced waveform quality, our work establishes the first step towards constructing waveform templates of BH binaries in non-vacuum environments, suitable for next-generation gravitational wave detectors. As a closing remark, we comment on the possibility of finding imprints of a massive scalar cloud in realistic astrophysical configurations, and the implications towards probing dark matter and ultralight scalars through strong gravity.

The paper is organized as follows: In Sec. II we describe the theoretical framework and initial value formulation. In Sec. III we discuss our approach construct constraint-satisfying initial data for the Einstein–Klein–Gordon equations. We summarize the numerical relativity framework in Sec. IV. In Sec. V we present results for our simulations of quasi-circular BH binaries embedded in a dark matter environment. We conclude in Sec VI.

Throughout this study, we use natural units where $G = c = 1$ and $\hbar = 1$, and we adopt the $(-, +, +, +)$ signature for the spacetime metric. We denote symmetrization and anti-symmetrization of a tensor by $A_{(\mu\nu)} = \frac{1}{2}(A_{\mu\nu} + A_{\nu\mu})$ and $A_{[\mu\nu]} = \frac{1}{2}(A_{\mu\nu} - A_{\nu\mu})$, respectively.

II. GENERAL RELATIVITY AND MASSIVE SCALARS

A. Action and equations of motion

We consider a complex, massive scalar field Φ minimally coupled to gravity, described by the action

$$S = \int d^4x \sqrt{-g} \left(\frac{(4)R}{16\pi} - \frac{1}{2} g^{\mu\nu} \nabla_\mu \Phi^\dagger \nabla_\nu \Phi - \frac{\mu_S^2}{2} \Phi^\dagger \Phi \right), \quad (2)$$

where Φ^\dagger is the complex conjugate of the scalar, and $\mu_S = m_S/\hbar$ is its mass parameter. We denote the four-dimensional spacetime metric, $g_{\mu\nu}$, its determinant $g = \det(g_{\mu\nu})$, the covariant derivative, ∇_μ , and Ricci scalar, $(4)R$, associated to the metric. Varying the action,

Eq. (2), yields the Einstein–Klein–Gordon equations

$$(4)R_{\mu\nu} - \frac{1}{2}g_{\mu\nu} (4)R = 8\pi T_{\mu\nu}, \quad (3a)$$

$$(g^{\mu\nu} \nabla_\mu \nabla_\nu - \mu_S^2) \Phi = 0, \quad (3b)$$

where $(4)R_{\mu\nu}$ is the Ricci tensor of the spacetime metric, and the scalar field energy-momentum tensor is

$$T_{\mu\nu} = \nabla_{(\mu} \Phi^\dagger \nabla_{\nu)} \Phi - \frac{1}{2}g_{\mu\nu} [\nabla^\alpha \Phi^\dagger \nabla_\alpha \Phi + \mu_S^2 \Phi^\dagger \Phi]. \quad (4)$$

We solve Eqs. (3) and (4) consistently to simulate the dynamical evolution of a coalescing BH binary and the surrounding scalar field condensate.

Note that we provide the action, field equations and time evolution equations (below) for a complex scalar field. In CANUDA, the complex scalar field is implemented as two real fields representing its real and imaginary part. Since their field equations decouple, CANUDA has the capability to evolve both a real or a complex scalar field. In this paper, we focus on a single real scalar. This corresponds to evolving the real part of Φ , while setting its imaginary part to zero throughout the simulations.

B. Time evolution formulation

To evolve Eqs. (3), we formulate them as an initial value problem. We first foliate the spacetime manifold, \mathcal{M} , into a family of spacelike hypersurfaces indexed by a time coordinate t . The geometry on each hypersurface is determined by the 3-dimensional, spatial metric, γ_{ij} . We introduce the unit timelike vector, n^μ , that is normal to the hypersurface. The spacetime coordinates are determined by the lapse function, α , and shift vector, β^i , that are collectively referred to as gauge functions. Putting all together, the spacetime metric can be expressed as

$$\begin{aligned} ds^2 &= g_{\mu\nu} dx^\mu dx^\nu \\ &= -(\alpha^2 - \beta_i \beta^i) dt^2 + 2\beta_i dt dx^i + \gamma_{ij} dx^i dx^j. \end{aligned} \quad (5)$$

In this coordinate system, the unit vector normal to each hypersurface has components $n^\mu = (1/\alpha, -\beta^i/\alpha)$ and $n_\mu = (-\alpha, \mathbf{0})$.

Using the 3+1 decomposition, the Einstein field equations can be rewritten in terms of 3-dimensional quantities, in the Arnowitt–Deser–Misner–York (ADM–York) formulation [77–79]. In this formulation, we introduce the extrinsic curvature,

$$K_{ij} = -\frac{1}{2} \mathcal{L}_n \gamma_{ij} = -\frac{1}{2\alpha} (\partial_t - \mathcal{L}_\beta) \gamma_{ij}, \quad (6)$$

where \mathcal{L}_n and \mathcal{L}_β denote the Lie derivatives along the normal vector n^μ and the shift vector β^μ , respectively. We note that the extrinsic curvature can be related to the conjugated momentum of the metric in the original

Hamiltonian formulation of Einstein's equations introduced by Arnowitt, Deser and Misner [77]. Similarly, we introduce the “momentum” of the scalar field Φ ,

$$\Pi = -\frac{1}{2}\mathcal{L}_n\Phi = -\frac{1}{2\alpha}(\partial_t - \mathcal{L}_\beta)\Phi, \quad (7)$$

and analogously for its complex conjugate. With these definitions, the time evolution of the spatial metric and of the scalar field is determined by

$$(\partial_t - \mathcal{L}_\beta)\gamma_{ij} = -2\alpha K_{ij}, \quad (8a)$$

$$(\partial_t - \mathcal{L}_\beta)\Phi = -2\alpha\Pi, \quad (8b)$$

and similarly for the scalar's complex conjugate. We obtain evolution equations for the extrinsic curvature and the scalar field “momentum” by decomposing the Einstein–Klein-Gordon equations (3), and taking their spatial projection. They are given by

$$(\partial_t - \mathcal{L}_\beta)K_{ij} = -D_i D_j \alpha + \alpha [R_{ij} + KK_{ij} - 2K_{ik}K^k] + 4\pi\alpha[\gamma_{ij}(S - \rho) - 2S_{ij}], \quad (9a)$$

$$(\partial_t - \mathcal{L}_\beta)\Pi = \alpha \left[K\Pi - \frac{1}{2}D^i D_i \Phi + \frac{1}{2}\mu_S^2 \Phi \right] - \frac{1}{2}D^i \alpha D_i \Phi, \quad (9b)$$

and analogously for its complex conjugate. Here, D_i and R_{ij} are the covariant derivative and Ricci tensor with respect to the spatial metric, γ_{ij} , and $K = \gamma^{ij}K_{ij}$ is the trace of the extrinsic curvature. The matter contribution is encoded in the energy density ρ , energy-momentum flux j_i and the spatial stress tensor S_{ij} with its trace $S = \gamma^{ij}S_{ij}$. They are determined by projections of the energy-momentum tensor. For a massive (complex) scalar field, it is given by Eq. (4), and we obtain

$$\rho = n^\mu n^\nu T_{\mu\nu} = 2\Pi^\dagger\Pi + \frac{\mu_S^2}{2}\Phi^\dagger\Phi + \frac{1}{2}D_k\Phi^\dagger D^k\Phi, \quad (10a)$$

$$j_i = -\gamma_i^\mu n^\nu T_{\mu\nu} = \Pi^\dagger D_i \Phi + \Pi D_i \Phi^\dagger, \quad (10b)$$

$$S_{ij} = \gamma_i^\mu \gamma_j^\nu T_{\mu\nu} = D_{(i}\Phi^\dagger D_{j)}\Phi - \frac{1}{2}\gamma_{ij}D^k\Phi^\dagger D_k\Phi + \gamma_{ij} \left(2\Pi^\dagger\Pi - \frac{\mu_S^2}{2}\Phi^\dagger\Phi \right). \quad (10c)$$

The evolution equations of the extrinsic curvature determine six of the ten independent components of Einstein's equations (3a). The remaining components give the Hamiltonian and momentum constraints,

$$\mathcal{H} = R - K_{ij}K^{ij} + K^2 - 16\pi\rho = 0, \quad (11a)$$

$$\mathcal{M}_i = D^k K_{ik} - D_i K - 8\pi j_i = 0, \quad (11b)$$

computed by contracting Eq. (3a) with the normal vector. They are coupled elliptic partial differential equations that have to be satisfied at all times in the continuum limit of the Einstein equations. Rather than enforcing the constraints at each time step, we adopt the

free-evolution approach, i.e., we solve the constraints only to obtain the initial data, and monitor the constraint violation throughout the evolution. We will describe our approach to solving the constraints in detail in Sec. III.

Although the ADM-York formulation provides a simple description of the Einstein's equations as a Cauchy problem, they are only weakly hyperbolic [80], and simulations become numerically unstable. Instead, we use the Baumgarte-Shapiro-Shibata-Nakamura (BSSN) formulation [81, 82], which is rendered strongly hyperbolic by introducing auxiliary variables and using the constraints.

We adopt the “W” version of the BSSN formulation [83], i.e., we decompose the physical metric into the conformal factor, $W \equiv \gamma^{-1/6}$, and the conformal metric

$$\tilde{\gamma}_{ij} = W^2 \gamma_{ij}. \quad (12)$$

The extrinsic curvature K_{ij} is split into its trace K and its conformal trace-free part \tilde{A}_{ij} ,

$$K = \gamma^{ij}K_{ij}, \quad \tilde{A}_{ij} = W^2 \left(K_{ij} - \frac{1}{3}\gamma_{ij}K \right). \quad (13)$$

We introduce the conformal connection function,

$$\tilde{\Gamma}^i = \tilde{\gamma}^{jk}\tilde{\Gamma}_{jk}^i = -\partial_k\tilde{\gamma}^{ik}, \quad (14)$$

where $\tilde{\Gamma}_{jk}^i$ is the Levi-Civita connection of the conformal metric $\tilde{\gamma}_{ij}$. We summarize the evolution equations of the BSSN variables and of the scalar field in the BSSN formulation in App. A.

We close the system of evolution by prescribing the moving puncture gauge [84, 85] for the gauge functions. That is, we employ the 1 + log slicing condition and the Γ -driver shift condition [86, 87],

$$\partial_t\alpha = \beta^k\partial_k\alpha - 2\alpha K, \quad (15a)$$

$$\partial_t\beta^i = \beta^k\partial_k\beta^i - \eta\beta^i + \frac{3}{4}\tilde{\Gamma}^i, \quad (15b)$$

where we choose $\eta = 1$ in our simulations.

C. Gravitational wave extraction

We extract GWs from our numerical simulations by computing the Newman-Penrose scalar ¹

$$\Psi_4 = C_{\mu\nu\rho\sigma} k^\mu \bar{m}^\nu k^\rho \bar{m}^\sigma, \quad (16)$$

that represents outgoing gravitational radiation. Here, $C_{\mu\nu\rho\sigma}$ is the Weyl curvature tensor and k^μ and \bar{m}^μ are vectors of a null tetrad $\{l^\mu, k^\mu, m^\mu, \bar{m}^\mu\}$ with vanishing inner products except for $-l^\mu k_\mu = m^\mu \bar{m}_\mu = 1$.

¹ We follow the notation of Ref. [88] throughout.

We construct the vectors of the null tetrad from

$$l^\mu = \frac{1}{\sqrt{2}}(n^\mu + u^\mu), \quad k^\mu = \frac{1}{\sqrt{2}}(n^\mu - u^\mu), \quad (17a)$$

$$m^\mu = \frac{1}{\sqrt{2}}(v^\mu + iw^\mu), \quad \bar{m}^\mu = \frac{1}{\sqrt{2}}(v^\mu - iw^\mu), \quad (17b)$$

where n^μ is the timelike unit normal vector, and $\{u^\mu, v^\mu, w^\mu\}$ are spatial vectors forming a Cartesian orthonormal basis². Asymptotically, they correspond to radial, polar and azimuthal normal vectors.

In practice, we use the gravito-electric and gravitomagnetic decomposition of the Weyl tensor; see standard textbooks, e.g., Refs. [88, 90, 91] for details. The gravito-electric and -magnetic fields are defined as

$$E_{\mu\nu} = C_{\mu\lambda\nu\rho} n^\lambda n^\rho, \quad B_{\mu\nu} = {}^*C_{\mu\lambda\nu\rho} n^\lambda n^\rho, \quad (18)$$

where ${}^*C_{\mu\nu\rho\sigma} = \frac{1}{2}\epsilon_{\rho\sigma}^{\kappa\lambda}C_{\mu\nu\kappa\lambda}$ is the dual Weyl tensor. The symmetries of the Weyl tensor imply that the gravito-electric and -magnetic fields are traceless, spatial and symmetric, i.e., $g^{\mu\nu}E_{\mu\nu} = 0 = g^{\mu\nu}B_{\mu\nu}$, $E_{\mu\nu}n^\nu = 0 = B_{\mu\nu}n^\nu$ and $E_{[\mu\nu]} = 0 = B_{[\mu\nu]}$. Conversely, the Weyl tensor can be reconstructed from [88]

$$\begin{aligned} C_{\mu\nu\rho\sigma} &= 2(l_{\mu[\rho}E_{\sigma]\nu} - l_{\nu[\rho}E_{\sigma]\mu}) \\ &\quad - 2(n_{[\rho}B_{\sigma]\kappa}\epsilon^{\kappa}_{\mu\nu} + n_{[\mu}B_{\nu]\kappa}\epsilon^{\kappa}_{\rho\sigma}), \end{aligned} \quad (19)$$

where $l_{\mu\nu} = \gamma_{\mu\nu} + n_\mu n_\nu$. Putting everything together and making spatial tensor components explicit, the desired Newman-Penrose scalar can be written as

$$\Psi_4 = (E_{ij} - iB_{ij})\bar{m}^i\bar{m}^j. \quad (20)$$

Finally, we express the gravito-electric and -magnetic fields in terms of the 3-metric, extrinsic curvature and projections of the energy-momentum tensor. Performing the 3+1 decomposition of Eqs. (18) and inserting Eqs. (9) and (11), we find

$$E_{ij} = [R_{ij} + KK_{ij} - K_{ik}K^k{}_j - 4\pi S_{ij}]^{\text{TF}}, \quad (21a)$$

$$B_{ij} = [\epsilon_i{}^{lm}(D_lK_{mj} - 4\pi\gamma_{jl}j_m)]^{\text{TF}}, \quad (21b)$$

where $\epsilon_{\mu\nu\rho} = n^\sigma\epsilon_{\sigma\mu\nu\rho}$ is the three-dimensional Levi-Civita tensor, and $[\dots]^{\text{TF}}$ denotes the tracefree part of a tensor with respect to the 3-metric.

In practice, we implement Eq. (20) after inserting Eqs. (17) and evaluating Eqs. (21), where the explicit expressions are given in Sec. 4 of Ref. [92]. We extract the multipoles of the scalar field and of the Newman-Penrose scalar on spheres of fixed radii r_{ex} . We interpolate the fields $f \in \{\Psi_4, \Phi\}$, on spheres of radii r_{ex} , and expand them as

$$f(t, r_{\text{ex}}, \theta, \varphi) = \sum_{\ell=0}^{\infty} \sum_{m=-\ell}^{\ell} f_{\ell m}(t, r_{\text{ex}}) {}_s Y_{\ell m}(\theta, \varphi), \quad (22)$$

where ${}_s Y_{\ell m}(\theta, \varphi)$ are the spin- s -weighted spherical harmonics. The spin-weight is $s = -2$ for the Newman-Penrose scalar Ψ_4 and $s = 0$ for the scalar field Φ . The (ℓ, m) multipole is computed by the projection

$$f_{\ell m}(t, r_{\text{ex}}) = \int d\Omega f(t, r_{\text{ex}}, \theta, \varphi) {}_s Y_{\ell m}^*(\theta, \varphi). \quad (23)$$

Finally, we compute the luminosity (i.e., energy flux) of the gravitational radiation using

$$\frac{dE_{\text{GW}}}{dt} = \lim_{r_{\text{ex}} \rightarrow \infty} \frac{r_{\text{ex}}^2}{16\pi} \sum_{\ell=2}^{\infty} \sum_{m=-\ell}^{\ell} \left| \int_{-\infty}^t dt' \Psi_{4,\ell m} \right|^2. \quad (24)$$

In practice, we sum over the first $\ell = 2, \dots, 8$ multipoles and compute the energy flux at $r_{\text{ex}} = 100M$.

III. INITIAL DATA FOR BLACK-HOLE BINARIES IMMERSED IN A SCALAR CLOUD

Constraint-satisfying initial data is key for a consistent time evolution. In fact, a simple superposition of scalar fields onto the metric introduces constraint violations that can yield incorrect physical results [93]. We derive the formulation of the initial data problem for binary BHs immersed in a scalar cloud in Sec. III A, and discuss its well-posedness in Sec. III B. The numerical implementation is presented in Sec. IV.

A. Constraints with scalar field contributions

We first need to construct constraint-satisfying initial data for the metric in the presence of a scalar cloud. Consistent initial data requires one to solve simultaneously for (i) constraint-satisfying metric data in the presence of the scalar and (ii) a quasi-equilibrium state of the scalar field. In this paper we focus on the first task, and solve the constraint equations for the metric using the conformal, transverse, traceless decomposition [78, 94, 95]. The scalar field source is set up via an approximate, analytic prescription. In particular, we leverage the result that simple scalar field profiles reach their equilibrium configuration around a BH binary within a few orbits [96].

Our method allows for a general scalar field profile, and only assumes that the field is momentarily at rest,

$$\Pi(t=0) = 0. \quad (25)$$

Then, the energy density and flux of the scalar field, Eqs. (10), reduce to

$$\rho = \frac{\mu_S^2}{2}\Phi^\dagger\Phi + \frac{1}{2}D^k\Phi^\dagger D_k\Phi, \quad (26a)$$

$$j_i = 0. \quad (26b)$$

With this choice, the momentum constraint (11b) reduces to that of vacuum General Relativity.

² In the code they are constructed following App. C of Ref. [89].

Next, we write the constraints, Eqs. (11), in the conformal, transverse, traceless decomposition [78, 94, 95], which prescribes a conformal rescaling of the metric and extrinsic curvature

$$\gamma_{ij} = \psi^4 \bar{\gamma}_{ij}, \quad K_{ij} = \psi^{-2} \bar{A}_{ij} + \frac{1}{3} \psi^4 \bar{\gamma}_{ij} K. \quad (27)$$

Here, ψ is the conformal factor, $\bar{\gamma}_{ij}$ is the conformal metric, and \bar{A}_{ij} is the traceless part of the conformal extrinsic curvature. We simulate asymptotically flat space-times, and we therefore impose the boundary condition $\lim_{r \rightarrow \infty} \psi = 1$.

We further simplify the constraint equations by imposing maximal slicing, $K = 0$, and conformal flatness, $\bar{\gamma}_{ij} = \eta_{ij}$ where $\eta_{ij} = \text{Diag}(1, 1, 1)$ is the flat spatial metric. With these assumptions and the conformal decomposition of Eq. (27), the constraint equations decouple and become

$$\bar{D}^i \bar{D}_i \psi + \frac{1}{8} \psi^{-7} \bar{A}_{ij} \bar{A}^{ij} + 2\pi \psi^5 \rho = 0, \quad (28a)$$

$$\bar{D}_j \bar{A}^{ij} = 0, \quad (28b)$$

where \bar{D} denotes the covariant derivative with respect to the conformal (flat) metric, and the density is now

$$\rho = \frac{\mu_S^2}{2} \Phi^\dagger \Phi + \frac{1}{2} \psi^{-4} \bar{\gamma}^{kl} \bar{D}_k \Phi^\dagger \bar{D}_l \Phi. \quad (29)$$

The momentum constraint, Eq. (28b), can be solved exactly by the Bowen-York extrinsic curvature [97]. For a single BH it is given by

$$\begin{aligned} \bar{A}_{ij}^{\text{BY}} &= \frac{3}{2r^2} [q_i P_j + q_j P_i + q^k P_k (q_i q_j - \eta_{ij})] \\ &\quad - \frac{3}{r^3} (\epsilon_{ikl} q_j + \epsilon_{jkl} q_i) q^k S^l, \end{aligned} \quad (30)$$

where q^i is an outward-pointing unit radial vector, $\epsilon_{\mu\nu\rho} = n^\sigma \epsilon_{\sigma\mu\nu\rho}$ is the Levi-Civita tensor in three dimensions, r the BH's position, and P^i and S^i are the ADM linear and angular momenta, respectively. Because the momentum constraint, Eq. (28b), is a linear differential equation, we obtain solutions for multiple BHs via a superposition of individual Bowen-York solutions as shown by Brandt & Brügmann [71].

With the momentum constraint solved analytically, all that remains is solving the Hamiltonian constraint, Eq. (28a). To this end, we adopt the puncture decomposition of the conformal factor [71],

$$\psi = \psi_{\text{BL}} + u, \quad \text{with} \quad \psi_{\text{BL}} = 1 + \sum_{a=1}^N \frac{m_{(a)}}{2|r - r_{(a)}|}, \quad (31)$$

where $m_{(a)}$ and $r_{(a)}$ are the mass parameter and position of the a -th BH, ψ_{BL} denotes the Brill-Lindquist solution (for time symmetric BH solutions in vacuum), and u is a C^2 function determining the correction to that solution.

Applying Eq. (31) and using $\bar{\gamma}_{ij} = \eta_{ij}$ explicitly, the Hamiltonian constraint becomes

$$\begin{aligned} 0 &= \Delta_\eta u + \frac{1}{8} (u + \psi_{\text{BL}})^{-7} \bar{A}_{ij} \bar{A}^{ij} \\ &\quad + \pi (u + \psi_{\text{BL}})^5 \mu_S^2 \Phi^\dagger \Phi + \pi (u + \psi_{\text{BL}}) \eta^{kl} \partial_k \Phi^\dagger \partial_l \Phi, \end{aligned} \quad (32)$$

where $\Delta_\eta = \eta^{ij} \partial_i \partial_j$ is the flat space Laplacian, and we insert the scalar's energy density.

Our strategy has reduced the initial data problem to solving one elliptic partial differential equation (PDE) for the function u . This approach captures a large class of interesting problems involving the interaction between BHs and scalar fields, as long as the scalar can be treated as (approximately) momententarily at rest. More demanding setups, such as superradiant quasi-bound states [7, 21] which are time-dependent, or highly spinning BHs (exceeding the spin bound of Bowen-York data [98, 99]) would entail solving the coupled momentum constraint equations [67, 100]. They are beyond the scope of the current work.

B. Well-posedness of the Hamiltonian constraint

With the formalism in hand, we implemented Eq. (32) in `TWO_PUNCTURES_BBHSF` (see Sec. IV B for details). The initial numerical solutions of BHs in the presence of a massive scalar field, appeared physical and reasonably well behaved. However, they failed to converge as we increased the resolution of the spectral solver.

This behavior is a strong indication for a numerical instability, and we identified the mathematical structure of Eq. (32) as its root. To see this, recall that a necessary condition for numerical stability is the well-posedness of the underlying PDE. Here, we are concerned with elliptic PDEs. They are well-posed if their linearized version,

$$\Delta \epsilon - h \epsilon = 0, \quad (33)$$

where ϵ is a small perturbation, satisfies $h > 0$ [101, 102].

Analysing Eq. (32), we find that the mass term $\sim \mu_S^2 (u + \psi_{\text{BL}})^5 \Phi^\dagger \Phi$ changes the sign of the function h to $h < 0$. That is, the mass term changes the elliptic character of the constraint, thus spoiling the convergence properties of our code. We cure this problem by conformally rescaling the scalar field as

$$\Phi = \psi^\delta \bar{\Phi}, \quad \Phi^\dagger = \psi^\delta \bar{\Phi}^\dagger, \quad (34)$$

where ψ is the conformal factor. The key idea is to choose the exponent δ such that $h > 0$ in the linearized equation. This corresponds to choosing δ such that all powers of the conformal factor in the Hamiltonian constraint become negative. After applying the rescaling, the Hamiltonian constraint, Eq. (32), becomes

$$0 = \Delta_\eta u + \frac{\bar{A}_{ij}\bar{A}^{ij}}{8(u + \psi_{\text{BL}})^7} + \pi(u + \psi_{\text{BL}})^{2\delta+5} \mu_S^2 \bar{\Phi}^\dagger \bar{\Phi} + \pi\delta(u + \psi_{\text{BL}})^{2\delta} (\partial^i u + \partial^i \psi_{\text{BL}}) (\bar{\Phi} \partial_i \bar{\Phi}^\dagger + \bar{\Phi}^\dagger \partial_i \bar{\Phi}) \\ + \pi(u + \psi_{\text{BL}})^{2\delta+1} (\partial^i \bar{\Phi})(\partial_i \bar{\Phi}^\dagger) + \pi\delta^2(u + \psi_{\text{BL}})^{2\delta-1} (\partial^i u + \partial^i \psi_{\text{BL}})(\partial_i u + \partial_i \psi_{\text{BL}}) \bar{\Phi}^\dagger \bar{\Phi}, \quad (35)$$

where we raise indices using the flat metric η^{ij} . The well-posedness of the elliptic equation can be shown by

linearizing Eq.(35) around a known solution u_0 . We introduce $u = u_0 + \epsilon$, with $|\epsilon| \ll |u_0|$, and expand Eq. (35) to first order in ϵ to find

$$0 = \Delta_\eta \epsilon - \frac{7\bar{A}_{ij}\bar{A}^{ij}}{8(u_0 + \psi_{\text{BL}})^8} \epsilon + \pi(u_0 + \psi_{\text{BL}})^{2\delta} [(2\delta + 1)(\partial^i \bar{\Phi}^\dagger)(\partial_i \bar{\Phi}) \epsilon + \delta(\bar{\Phi} \partial^i \bar{\Phi}^\dagger + \bar{\Phi}^\dagger \partial^i \bar{\Phi})(\partial_i \epsilon)] \\ + \pi(2\delta + 5)\mu_S^2 |\bar{\Phi}|^2 (u_0 + \psi_{\text{BL}})^{2\delta+4} \epsilon + 2\pi\delta^2(u_0 + \psi_{\text{BL}})^{2\delta-1} (\partial^i u_0 + \partial^i \psi_{\text{BL}}) [(\bar{\Phi} \partial_i \bar{\Phi}^\dagger + \bar{\Phi}^\dagger \partial_i \bar{\Phi}) \epsilon + |\bar{\Phi}|^2 (\partial_i \epsilon)] \\ + \pi(2\delta - 1)\delta^2 |\bar{\Phi}|^2 (u_0 + \psi_{\text{BL}})^{2\delta-2} (\partial^i u_0 + \partial^i \psi_{\text{BL}})(\partial_i u_0 + \partial_i \psi_{\text{BL}}) \epsilon. \quad (36)$$

This can be brought (approximately) into the form of Eq. (33). Then, the existence of a unique solution requires that $h > 0$ [101, 102]. Since the function h is rather complicated we focus on the term with the largest power of the conformal factor. This corresponds to the term $\sim \mu_S^2$, and it becomes negative when $\delta < -5/2$. In practice, we set $\delta = -3$ in our simulations. We verified that different values $\delta \leq -3$ yield stable and unique solutions. Furthermore, the conformal rescaling implies regularity at the punctures, since the (physical) scalar field vanishes when approaching the punctures' positions by virtue of Eq. (34).

C. Initial scalar field profile

We initialize the (conformally rescaled) scalar field as a Gaussian shell that is momentarily at rest,

$$\bar{\Phi}(t=0) = A_{\text{SF}} Z(\theta, \phi) \exp\left[-\frac{(r - r_0)^2}{w^2}\right], \quad (37a)$$

$$\bar{\Pi}(t=0) = 0, \quad (37b)$$

where A_{SF} is the amplitude, r_0 and w are the peak position and width of the Gaussian, and $Z(\theta, \phi)$ indicates the field's angular distribution. In the code we implemented the options to set $Z(\theta, \phi) = Y_{00}(\theta, \phi)$ or $Z(\theta, \phi) = Y_{11}(\theta, \phi)$, where Y_{lm} are spherical harmonics. In this paper we always set $Z(\theta, \phi) = Y_{00}(\theta, \phi) = 1/\sqrt{4\pi}$.

IV. NUMERICAL RELATIVITY FRAMEWORK

To simulate binary BHs immersed in a scalar cloud, we extend and use the EINSTEIN TOOLKIT [73, 74] alongside

the CANUDA code [76, 103]. We summarize the software in Sec. IV A, and describe our new initial data solver in Sec. IV B. In Sec. IV C we list the simulations performed for this paper and summarize their setup.

A. Software description

We perform simulations with the EINSTEIN TOOLKIT, an open-source software for numerical relativity and computational astrophysics [73, 74]. The toolkit consists of a set of “arrangements” that, in turn, are a collection of “thorns” which implement specific physics or infrastructure tasks. The EINSTEIN TOOLKIT is based on the CACTUS computational toolkit [104, 105] and the CARPET boxes-in-boxes adaptive mesh refinement (AMR) driver [106, 107]. In addition to AMR, it also provides thorns for I/O and MPI/OpenMP hybrid parallelization.

The physics modules for this project are provided by our open-source CANUDA code for numerical relativity in fundamental physics [103]. We use the SCALAR arrangement with its initial data and scalar evolution thorns [93, 108], and the spacetime evolution and wave extraction thorns in the LEAN_PUBLIC arrangement.

We construct constraint-satisfying initial data of binary BH immersed in a massive scalar cloud with our new initial data solver TWO PUNCTURES_BBHSF [72]. It is an extension of the TWO PUNCTURES spectral solver [109]. We present a detailed description of TWO PUNCTURES_BBHSF, code validation and convergence tests in Sec. IV B below. We determine the BHs' initial momenta needed for a quasi-circular inspiral with the NRPyPN script [110, 111]. We evolve the coupled scalar and metric equations in the BSSN formulation [81, 82] together with the moving puncture gauge [84–86] as sum-

marized in App. A. The metric evolution equations are implemented in the LEANBSSNMoL thorn, while the scalar's evolution is carried out with the SCALAR-EVOLVE thorn. The latter also computes the components of the scalar field's energy-momentum tensor that are stored in the TMUNUBASE thorn. To couple the scalar field to the metric, LEANBSSNMoL reads the components of the energy-momentum tensor from TMUNUBASE.

The equations are numerically integrated via the method of lines. We calculate spatial derivatives using finite differences. We upgraded both evolution thorns to provide up to eighth order finite difference stencils that are centered for all regular evolution variables and lopsided for advection derivatives $\sim \partial_k \beta^k$. We add artificial Kreiss-Oliger dissipation to reduce high-frequency noise that is generated at mesh refinement boundaries. The simulations presented here use eighth order finite difference stencils for spatial derivatives together with ninth order stencils for the dissipation and a dissipation coefficient $\epsilon_{\text{diss}} = 0.325$. We adopt Sommerfeld, i.e., radiative boundary conditions for both the metric and scalar field [86]. We integrate the evolution equations with a fourth order Runge-Kutta integrator. The EINSTEIN TOOLKIT uses subcycling in time, and the time step on each refinement level is determined by the Courant factor which we typically set to $dt/dx = 0.45$.

We compute two types of observables, namely the gravitational and scalar radiation generated by the coalescence, and (local) properties of the BHs. Information on the gravitational radiation is contained in the Newman-Penrose scalar Ψ_4 ; see Sec. II C. To compute the Newman-Penrose scalar in the presence of the scalar field, we extend CANUDA's wave extraction thorn NPSCALARS. The updated NPSCALARS thorn reads the energy-momentum tensor from the TMUNUBASE thorn, constructs the energy density, energy-momentum flux and spatial stress, and incorporates them via Eqs. (21). We further upgraded NPSCALARS by implementing up to eighth order finite difference stencils to compute Ψ_4 . We perform a multipolar decomposition of the Newman-Penrose scalar and of the scalar field (c.f. Eq. (23)) using the MULTIPOLE thorn.

We compute (local) properties of the individual and final BHs using the QUASILOCALMEASURES thorn [112], and their apparent horizons with the AHFINDERDIRECT thorn [113]. These include the apparent horizons' area A_{AH} , equatorial circumference C_e , and irreducible mass $M_{\text{irr}} = \sqrt{A_{\text{AH}}/(16\pi)}$. The latter are used to compute the BHs' dimensionless spin

$$\chi \equiv \frac{J}{M_{\text{BH}}^2} = \sqrt{1 - \left(\frac{2\pi A_{\text{AH}}}{C_e^2} - 1 \right)^2}, \quad (38)$$

and mass according to Christodoulou's formula,

$$M_{\text{BH}}^2 = M_{\text{irr}}^2 + \frac{J^2}{4M_{\text{irr}}^2}. \quad (39)$$

B. Initial data solver: TwoPUNCTURES_BBHSF

We have designed the initial data routine TwoPUNCTURES_BBHSF [72] to prepare constraint-satisfying initial configurations of binary BHs surrounded by a massive scalar field. It is public as a new thorn of the SCALAR arrangement [76]. We base TwoPUNCTURES_BBHSF on the TwoPUNCTURES pseudo-spectral solver [109], for conformally flat binary BH initial data [71]. In particular, we implement Eqs. (35) and (36), while leaving TwoPUNCTURES's underlying infrastructure unchanged. The solver employs pseudo-spectral methods, and expands the solution in the basis of Chebyshev or (for the azimuthal coordinate) Fourier polynomials.

The accuracy of a solution is determined by the number of collocation points (N_A, N_B, N_φ) , i.e., the number of terms in the series expansion. We validate the code by performing a convergence analysis. To do so, we fix the number of collocation points in the azimuthal coordinate, $N_\varphi = 24$, and vary $N_A = N_B = N$. We set the solution u_{160} with $N = 160$ as our reference solution, and define the relative error

$$\Delta_{N,160} = \max \left(1 - \frac{u_N}{u_{160}} \right), \quad (40)$$

where u_N denotes solutions constructed with a lower resolution $N < 160$.

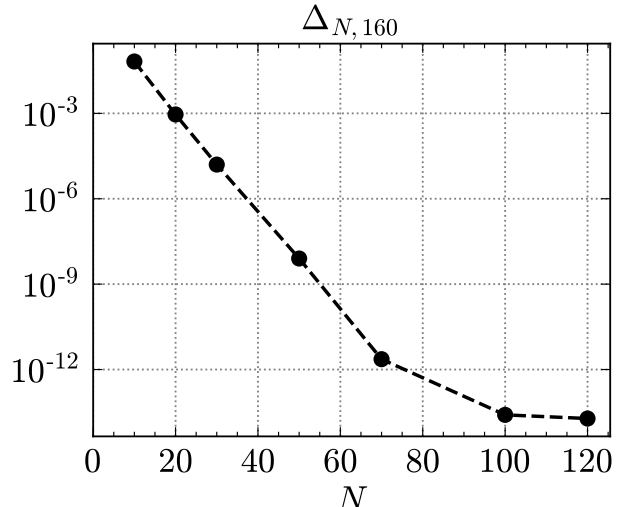


FIG. 2. Convergence plot for TwoPUNCTURES_BBHSF, computing the initial solution of a binary BH with mass ratio $q = 1/2$ immersed in a scalar cloud with mass parameter $M\mu_S = 0.4$; run **q12mu04** in Table I. We show the relative error $\Delta_{N,160}$ between a solution u_N obtained with N collocation points and the reference solution u_{160} , as a function of the number of collocation points N .

We perform the convergence test for run **q12mu04**, which is one of the most demanding setups in our pool of simulations listed in Table I. The run represents a binary

BH with a mass ratio $q = M_1/M_2 = 1/2$ surrounded by a scalar cloud with mass parameter $M\mu_S = 0.4$. We construct this setup's initial solution, u_N , with a series of collocation points $N \in \{10, 120\}$, and compute the relative error defined in Eq. (40). Specifically, we compute the relative error along the x -axis, and its maximum typically corresponds to the position of the punctures. The results are presented in Fig. 2. With increasing number of collocation points N , the relative error, $\Delta_{N,160}$, decays exponentially until about $N \sim 100$, and then saturates. This cross-over from exponential to algebraic convergence is already present in the original TWOPOUNC-TURES solver, and it is due to the solution's logarithmic fall-off at infinity [109].

For all simulations in this paper, we choose $N = 80$ and $N_\varphi = 24$ for which we still obtain exponential convergence and the relative error is $\Delta_{N=80,160} \lesssim 10^{-12}$.

C. Simulation setup

We perform a simulation campaign to determine the impact of a scalar condensate on the dynamics of coalescing binary BHs and their gravitational-wave emission, as sketched in Fig. 1 and summarized in Table I.

We set up binaries of quasi-circular, nonspinning BHs with ADM masses $M_{1,2}$, total mass $M = M_1 + M_2 = 1$, and mass ratios $q = M_1/M_2 = 1, 1/2$. The BHs have an initial separation of $d = |x_1 - x_2| = 10M$. The binary is initially surrounded by a spherically symmetric scalar condensate with a Gaussian radial profile of the conformal scalar field, $\bar{\Phi}$, given by Eq. (37), and angular profile $Z(\theta, \varphi) = Y_{00}(\theta, \varphi) = 1/\sqrt{4\pi}$. The Gaussian is centered around the origin, $r_0 = 0$, has a width of $w = 10M$, and the amplitude A_{SF} is chosen such that the maximum of the energy density (in flat space) is about $\bar{\rho}_{\max}M^2 = 1.6 \times 10^{-7}$.

There are two factors determining our choice of the initial energy density. The first, perhaps more practical reason, is that the scalar cloud density should be sufficiently large to have a measurable impact on the binary. On the other hand, our choice has to be astrophysically viable, i.e., it should be below the maximum density that can be reached through known enhancement mechanisms. To connect with astrophysical estimates, we convert the energy density between geometric units used in numerical relativity and physical units according to

$$\rho_{\text{NR}}M^2 = 10^{-28} \left(\frac{\rho}{M_\odot/\text{pc}^3} \right) \left(\frac{M_{\text{BH}}}{10^6 M_\odot} \right)^2. \quad (41)$$

The average galactic dark matter abundance is about $\rho_{\text{gal}} \sim 0.01 M_\odot/\text{pc}^3$ [9]. In other words, the corresponding value in geometric units is $\rho_{\text{NR,gal}}M^2 \sim 10^{-30}(M_{\text{BH}}/10^6 M_\odot)^2$, and therefore negligible in our simulations. However, enhancement mechanisms such as the superradiant growth of a bosonic cloud can carry as much as 10% of the BH mass [24, 28, 29]. Fur-

Name	q	$M\mu_S$	A_{SF}/M	λ_r	λ_t	M_{ADM}/M	ϵ_Ω
q1vac	1	NA	NA	1	1	0.9898	0.0041
q1mu00	1	0.0	0.0233	0.5	1	0.9906	0.0089
q1mu02	1	0.2	0.0100	0.8	1	0.9902	0.0010
q1mu04	1	0.4	0.0050	1	1	0.9901	0.0029
q1mu06	1	0.6	0.0033	1	1.001	0.9901	0.0089
q1mu08	1	0.8	0.0025	1	1.001	0.9906	0.0091
q1mu10	1	1.0	0.0020	1	1.001	0.9901	0.0089
q12vac	1/2	NA	NA	1	1	0.9909	0.0051
q12mu00	1/2	0.0	0.0233	0.84	1.001	0.9918	0.0013
q12mu02	1/2	0.2	0.0100	0.90	1.001	0.9913	0.0009
q12mu04	1/2	0.4	0.0050	1.12	1.001	0.9912	0.0048
q12mu06	1/2	0.6	0.0033	1.12	1.001	0.9912	0.0045
q12mu08	1/2	0.8	0.0025	1.12	1.001	0.9912	0.0047
q12mu10	1/2	1.0	0.0020	1.12	1.001	0.9912	0.0046

TABLE I. Summary of the initial binary BH and scalar field parameters. We report the name of the simulation, the BHs' mass ratio $q = M_1/M_2 \leq 1$, the scalar's (dimensionless) mass parameter $M\mu_S$ and amplitude A_{SF} , eccentricity reduction parameters λ_r and λ_t , ADM energy M_{ADM} , and eccentricity ϵ_Ω . We choose the scalar's amplitude A_{SF} such that its maximum energy density (in the flat space approximation) is $\bar{\rho}_{\max}M^2 = 1.6 \times 10^{-7}$. The initial momenta in vacuum are set to $(P_r^{(0)}, P_t^{(0)}) = (-0.101, 9.63) \times 10^{-2}M$ for **q1vac**, and $(P_r^{(0)}, P_t^{(0)}) = (-0.071, 8.557) \times 10^{-2}M$ for **q12vac**. In simulations with the scalar field, we apply the eccentricity reduction parameters and set the initial momenta to $(P_r, P_t) = (\lambda_r P_r^{(0)}, \lambda_t P_t^{(0)})$.

thermore, when combined with accretion [30], superradiance can increase the energy density up to $\rho_{\text{NR,SR}}M^2 \sim 10^{-5}(M_{\text{BH}}/10^6 M_\odot)^2$ in geometric units [24]. With these considerations, the energy density chosen in our simulations, $\bar{\rho}_{\max}M^2 = 1.6 \times 10^{-7}$, may therefore represent a superradiant cloud around a supermassive BH.

We perform a series of binary BH simulations, varying the scalar field's dimensionless mass parameter in the range $M\mu_S \in \{0, 0.2, 0.4, 0.6, 0.8, 1\}$ for each mass ratio $q \in \{1, 1/2\}$. The simulation suite is summarized in Table I. We list the selection of the initial BH and scalar field parameters, the binaries' ADM mass, initial momenta and eccentricity.

To identify the effect of a scalar field environment, we need to compare the evolution of quasi-circular binaries – of comparable, low eccentricities – in the presence of scalar matter against those in vacuum. However, even in a consistent solution of the constraint equations, the scalar cloud can yield different initial BH parameters and, thus, introduce artificially eccentric orbits that are due to the initial conditions rather than being a signature of dark matter [96]. To rule out this effect, we therefore use an iterative procedure to reduce the binaries' eccentricity. Guided by state-of-the-art in vacuum binary BH simulations, we aim at generating initial configurations with an eccentricity $\epsilon_\Omega \lesssim 9 \times 10^{-3}$.

In vacuum spacetimes, low eccentricity is achieved by setting the BHs' momenta from post-Newtonian approximations, estimating the binary's eccentricity after evolving it for a few orbits and correcting the holes' momenta [114] iteratively until the target eccentricity is met.

For binary BHs surrounded by a scalar condensate, we adjust this procedure as follows:

- (i) We set the initial guess of the BHs' linear momenta with the NRPyPN code [110], based on Post-Newtonian calculations of quasi-circular binaries in vacuum [114–117]. We set the tangential and radial components of the initial momenta for an equal-mass binary with separation $d = 10M$ to $P_t^{(0)} = 9.63 \times 10^{-2}M$ and $P_r^{(0)} = 1.01 \times 10^{-3}M$. For the binary with mass ratio $q = 1/2$ we set $P_t^{(0)} = 8.557 \times 10^{-2}M$ and $P_r^{(0)} = 7.1 \times 10^{-4}M$.
- (ii) We initialize the conformal scalar field as a Gaussian using Eq. (37) with $Z(\theta, \varphi) = 1/\sqrt{4\pi}$, $r_0 = 0$, $w = 10M$, and A_{SF} and $M\mu_S$ given in Table I.
- (iii) We solve the constraints for the initial metric and extrinsic curvature using `TWOPUNCTURES_BBHSF` with the initial parameters set in steps (i) and (ii); see Sec. III.
- (iv) We evolve the initial data for several orbits. After the gauge adjustment (present in the first $\sim 200M$) we compute the eccentricity estimator [114]

$$\epsilon_\Omega = \frac{\Omega(t) - \Omega(\epsilon = 0)}{2\Omega(\epsilon = 0)}. \quad (42)$$

It is a measure for the time dependent oscillations of the orbital frequency $\Omega(t)$ relative to the frequency of a circular orbit $\Omega(\epsilon = 0)$. The former is computed from the coordinate separation. The latter is obtained by fitting the numerical data assuming a quasi-circular ansatz for Ω from PN expansions, and averaging any eccentricity or gauge effects. For more details Sec. IIIB of Ref. [114].

- (v) Based on the eccentricity estimate in Eq. (42), we correct the initial linear momenta as $P_{t,r} \rightarrow \lambda_{t,r} P_{t,r}$, and then recompute the initial data. We repeat steps (iii) – (iv), each time choosing a different set of correction factors $\lambda_{t,r}$ (by trial-and-error), until the eccentricity satisfies $\epsilon_\Omega \lesssim 9 \times 10^{-3}$. In the simulations presented here, we typically need 3-5 iterations to reach the eccentricity threshold.

With the initial data carefully set up to represent low eccentricity, quasi-circular binary BHs, we turn our attention to the evolution. All simulations presented here employ eighth order finite difference stencils.

The simulation domain consists of a three-dimensional Cartesian grid with an extent of $\sim 512M$ in each dimension, where M is the total mass in the spacetime. In order to sufficiently resolve the BH horizons, we aim for a grid spacing finer than $M/64$ at each of the BHs, and to make the simulation computationally feasible we employ 7 levels of moving, box-in-box style mesh refinement using the

CARPET driver [106]. The grid resolution on the outermost refinement level is $\Delta x_c = 0.854M$, corresponding to a grid spacing of $0.854M/2^6 \sim 1/75M$ at the center of the BHs. We provide a full suite of convergence tests in App. B, with relative error of $< 4\%$ for the modulus and $< 0.3\%$ for the complex phase of $\Psi_{4,22}$.

V. RESULTS

A. Evolution of the binary-cloud system

We illustrate the evolution of a BH binary immersed in a scalar cloud in Fig. 3, exemplarily for the simulation **q12mu04** in Table I. We present a series of two-dimensional pseudocolor plots displaying, from left to right, the scalar energy density, scalar and gravitational radiation in the BHs' orbital plane. We overlay the scalar's density with circles indicating the position and mean radius of the BHs' apparent horizons. From top to bottom, the snapshots show (1) the initial transient, (2) the binary's evolution after about 1.5 orbits, (3) the binary about 0.5 orbits before the BHs merge, and (4) about $130M$ after the merger. The complete animation is available on our CANUDA youtube channel [118].

As the BH binary begins its quasi-circular inspiral, the initially spherically-symmetric scalar cloud is stirred up and accreted onto the individual BHs, forming a pair of scalar overdensities trailing the BHs. The overdensities are consistent with transient scalar “charges” found for single BHs immersed in a time-dependent scalar field [18, 19, 93]. We find that in the binary they act like charges and, through their motion along with the BHs, they generate scalar radiation. The snapshot of the Newman-Penrose scalar depicts a burst of initial “junk” radiation that is a known artifact of puncture initial data [110, 119]. As the BHs progress through their inspiral, the scalar “charges” produce scalar dipole radiation shown in the top two rows of Fig. 3. The gravitational radiation increases in frequency and amplitude, although too faint to be visible in the snapshot in the second row. As the BHs merge, a burst of gravitational radiation is emitted, after which the final rotating BH rings down. The scalar forms a slowly decaying cloud anchored around the final BH. We also note an interference pattern due to boundary effects.

Compared to a binary BH coalescence in vacuum, the presence of a massive scalar condensate may accelerate or slow down the coalescence. The change in merger time manifests as a phase shift in the gravitational radiation. The emission of scalar radiation and accretion of the scalar field on to the BH can both accelerate the coalescence. On the other hand, the BHs may experience a delay in the merger under the effects of dynamical friction from the scalar cloud.

In the following, we focus on simulations with scalar mass parameters $M\mu_S \in \{0.2, 0.4, 0.6\}$ as a representative sample, for both BH mass ratios.

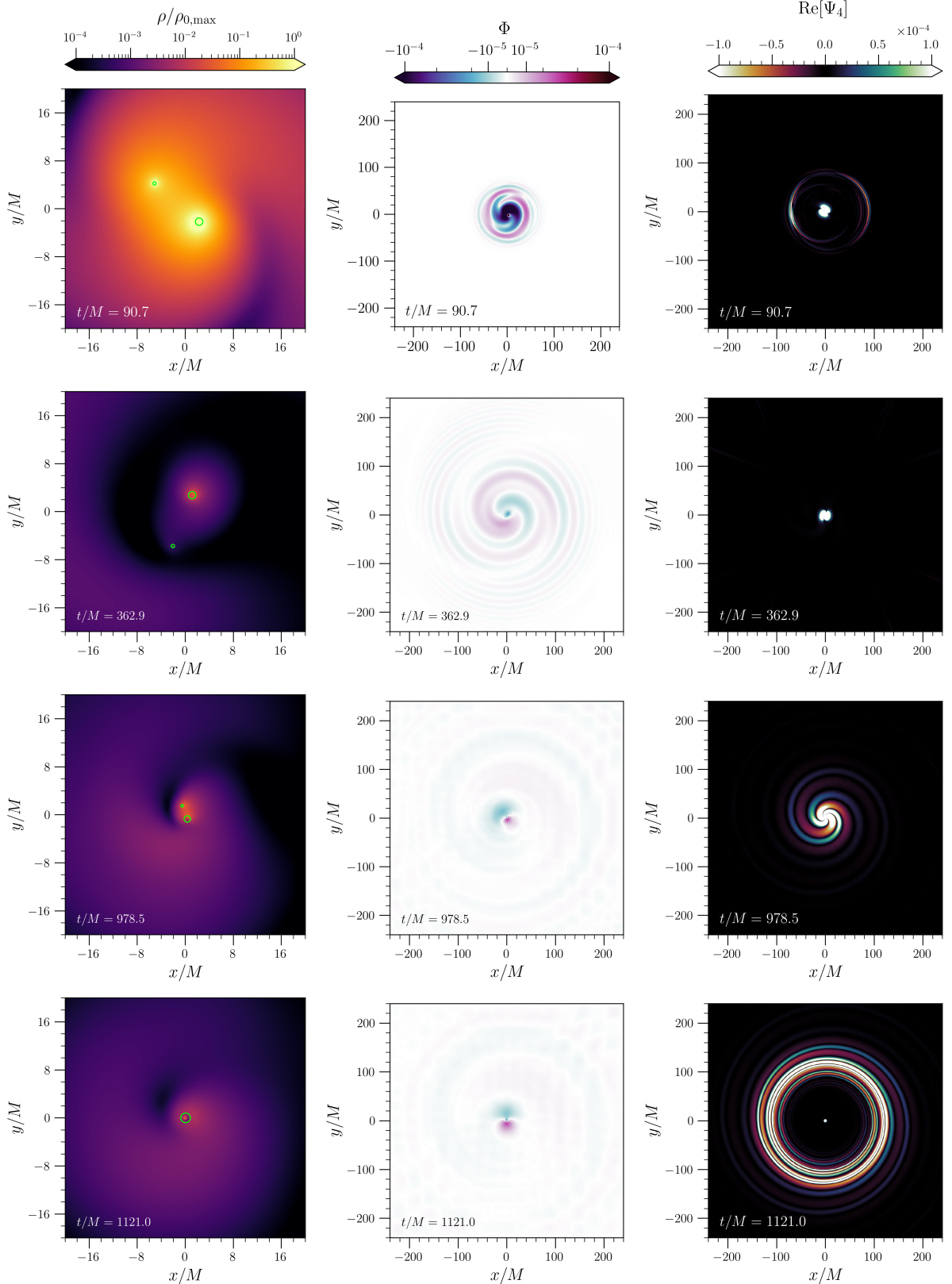


FIG. 3. Two-dimensional snapshots of the simulation **q12mu04**. From left to right, the pseudocolor plots show the scalar's energy density ρ normalized by the initial maximum value $\rho_{0,\max} = 1.6 \times 10^{-7} M^{-2}$ (left), the scalar field Φ (middle), and real part of the Newman-Penrose scalar Ψ_4 (right). The green circles in the left column indicate the locations and radii of the BHs' apparent horizons. From top to bottom we display these quantities at different stages of the binary's coalescence: (1) shortly after initial data settles and a burst junk radiation is emitted, (2) 1.5 orbits after the beginning of the simulation, (3) 0.5 orbit before merger, and (4) $\sim 130M$ after the merger. Note the difference in the displayed spatial domain, chosen to highlight features of the quantities.

B. Evolution of black hole properties

The energy density profile shown in Fig. 3, a steep gradient peaking at the location of the BHs is formed within the first two orbits. This sharp profile persists up until just before the merger. As the scalar overdensities accumulate around each BH, a fraction of the field is accreted onto the holes and increases their masses. The increase depends on the gravitational coupling, $M_{(a)}\mu_S$, between the scalar and individual BHs listed in Table II.

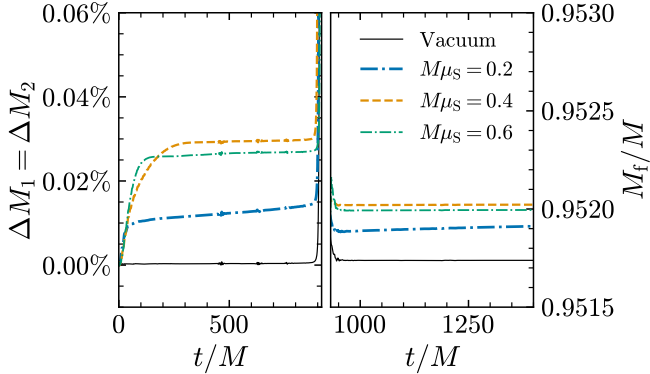


FIG. 4. Evolution of the Christodoulou mass, Eq. (39), for a BH binary with $q = 1$ and scalar mass parameters $M\mu_S$. The reference simulation in vacuum is indicated by the solid black line. Left: Percent change of the individual BHs' masses compared to their initial values. Right: Mass of the final BH.

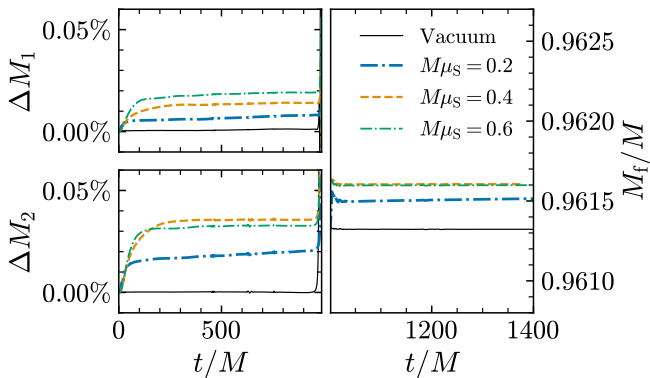


FIG. 5. Same as Fig. 4 but for mass ratio $q = 1/2$. Left: Percent change of the mass of BH 1 (top) and BH 2 (bottom) relative to their initial masses. Right: Mass of the final BH.

We see the accretion more clearly in Figs. 4 and 5, where we show the evolution of the Christodoulou mass, defined in Eq. (39), of the individual and of the final BHs in binaries with mass ratio $q = 1$ and $q = 1/2$, respectively. The masses of the individual BHs grow during their first orbit as the scalar cloud transitions from its initial, spherically symmetric configuration to the scalar “charges” around each BH. Following the early transition, the BHs' masses increase only very slowly throughout

the inspiral. This is consistent with the snapshots in Fig. 3, where the energy density relaxes to a nearly constant profile in the BHs' vicinity.

In the case of the equal-mass binary, the growth is around 0.01% to 0.03% of the initial BH masses depending on the scalar field mass parameter, and this percentage increase is consistent with the mass of the final BH. Albeit small, the increase is above the numerical error of about 0.001%; see App. B. The increase is largest for $M\mu_S = 0.4, 0.6$ which correspond to a gravitational coupling of $M_{(a)}\mu_S = 0.2, 0.3$ between the scalar and individual BHs, as listed in Table II. For the $q = 1/2$ binary, the more massive BH experiences a higher increase in its mass of up to 0.04%. Similar to the equal-mass case, the growth is only prominent during the first orbit, and it tapers off for the remainder of the inspiral. The mass of the final BH in the presence of a massive scalar cloud is about 0.02% larger than in the vacuum case.

The amount by which the BH masses increase is linked to the gravitational coupling, $M_{(a)}\mu_S$, between the scalar and the individual BHs. We find that a larger gravitational coupling $M_{(a)}\mu_S$ yields a larger increase in the BHs masses due to partial accretion of the surrounding scalar field. This is consistent with studies of single BHs, where the flux of scalar field into the BH increases with the scalar's mass parameter [19].

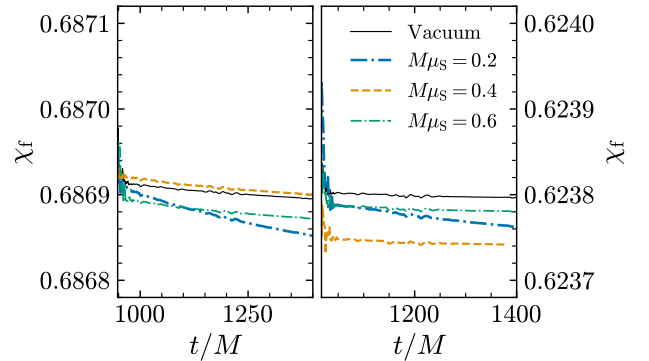


FIG. 6. Dimensionless angular momentum $\chi_f \equiv J/M_{\text{BH}}^2$ of the final BH in the equal-mass (left panel) and $q = 1/2$ (right panel) simulations.

The individual BHs were initialized as non-spinning BHs, and their spins remain zero throughout the inspiral. This is consistent with the scalar field being initialized as spherically symmetric Gaussian with zero angular momentum. Therefore, we only present the dimensionless spin of the final BH in Fig. 6. We find that its dimensionless spin is $\chi_f = 0.687$ for $q = 1$ and $\chi_f = 0.6238$ for $q = 1/2$. There is also little change in final spin among the scalar clouds with different mass parameter $M\mu_S$, which are well comparable with numerical error.

In conclusion, the initially spherically symmetric scalar field forms overdensities around each of the BHs in the early inspiral, a small fraction of which is accreted onto the BHs and increases their masses by about $\lesssim 0.05\%$.

Name	$M_1\mu_S$	$M_2\mu_S$	t_{merger}/M	$\Delta\phi_{22}$	$M\omega_{22}^{\text{peak}}$	E_{GW}/M
q1vac	NA	NA	907.7	0.00	0.28	0.0386
q1mu00	0.0	0.0	905.0	-1.36	0.28	0.0386
q1mu02	0.1	0.1	905.0	-1.35	0.28	0.0386
q1mu04	0.2	0.2	900.0	-3.74	0.29	0.0386
q1mu06	0.3	0.3	911.9	2.18	0.27	0.0386
q1mu08	0.4	0.4	911.6	2.03	0.28	0.0386
q1mu10	0.5	0.5	912.3	2.28	0.27	0.0386
q12vac	NA	NA	977.3	0.00	0.30	0.0300
q12mu00	0.0	0.0	987.2	4.39	0.29	0.0300
q12mu02	0.07	0.13	988.4	4.83	0.29	0.0300
q12mu04	0.13	0.27	983.8	2.95	0.29	0.0300
q12mu06	0.20	0.40	983.0	2.73	0.30	0.0300
q12mu08	0.27	0.53	983.8	2.80	0.29	0.0300
q12mu10	0.33	0.67	983.4	2.75	0.29	0.0300

TABLE II. Summary of the results. We report the name of the simulation, gravitational coupling $M_{(a)}\mu_S$ between the a -th individual BH and the scalar field, merger time t_{merger} determined by the formation of the common apparent horizon, GW phase shift $\Delta\phi_{22}$, peak frequency $\omega_{22}^{\text{peak}}$, and energy radiated gravitationally E_{GW} .

C. Scalar radiation

We observe that the scalar field builds up overdensities around the BHs in the early inspiral. Most of the overdensities remain anchored around each BH and decay very slowly. That is, for a transition period longer than the simulations, the field acts like a binary of scalar “charges” that follow the BHs’ coalescence. Through their motion, the “charges” generate scalar radiation as shown in the middle column of Fig. 3.

We present the evolution of the scalar’s multipoles up to $\ell = 2$ in Figs. 7 and 9, and their frequency spectra in Figs. 8 and 10, for the simulations with mass ratios $q = 1$ and $q = 1/2$, respectively. We rescale the multipoles by the extraction radius $r_{\text{ex}} = 100M$ to account for the r^{-1} radial falloff, and shift the time coordinate $\hat{t} \equiv t - r_{\text{ex}}$ to account for the time to propagate to the extraction sphere. We indicate the time of merger, determined by the formation of the common apparent horizon and listed in Table II, for the reference simulation in vacuum.

We first focus on the scalar’s monopole that indicates the scalar “charge” enclosed in the sphere of radius r_{ex} . In both sets of binary BH simulations and for all scalar field mass parameters, we see that the monopole oscillates with a frequency $\omega_R \sim \mu_S$ (c.f. top panels of Fig. 8 and 10) and its amplitude slowly decreases as a function of time (c.f. top panels of Fig. 7 and 9). We also observe that the overall magnitude of the monopole decreases as the scalars’ mass parameter increase. This trend can be understood from the construction of the initial profile: we fixed the scalars’ maximum energy density (instead of the amplitude), so scalar fields with a larger mass pa-

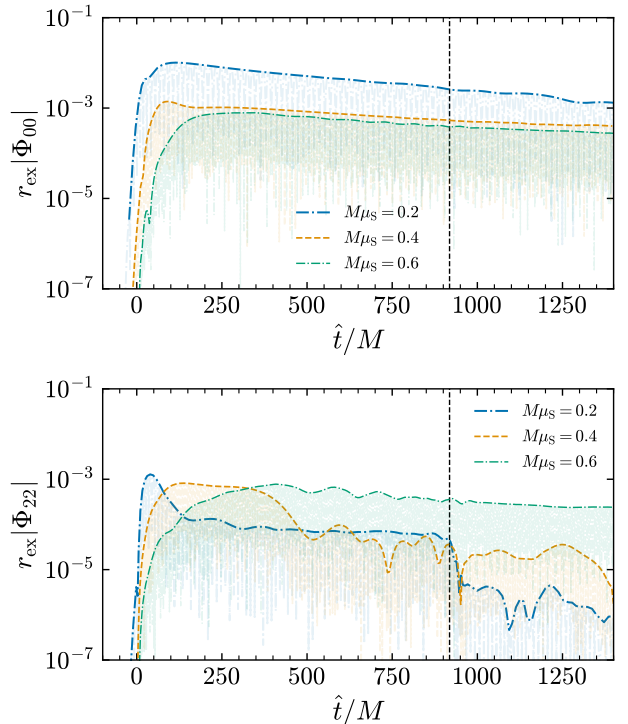


FIG. 7. Scalar field $\ell = m = 0$ (top panel) and $\ell = m = 2$ (bottom panel) multipoles, extracted at $r_{\text{ex}} = 100M$, for equal-mass binaries and different scalar mass parameters. The thick lines are the envelopes of $|\Phi_{\ell m}|$. The vertical lines indicate the merger time of the reference (vacuum) simulation.

rameter were initialized with a smaller amplitude and hence smaller initial scalar monopole.

We now turn to the scalar radiation. The leading contribution in the equal-mass BH binary is the $\ell = m = 2$ quadrupole shown in the bottom panel of Fig. 7 while the dipole is absent due to symmetry. In case of the mass parameter $M\mu_S = 0.2$ we see that, after an initial transient, the amplitude is approximately constant throughout the inspiral and rapidly decays after the BHs have merged. For $M\mu_S = 0.4$ we observe an almost constant amplitude for the first $t \sim 500M$, corresponding to about 2.5 orbits, before the quadrupole’s magnitude drops by an order of magnitude and slowly decays. In case of $M\mu_S = 0.6$, the amplitude of the quadrupole remains approximately constant throughout the simulations.

The bottom panel of Fig. 8 presents the frequency spectra of the scalar’s quadrupole before and after the BHs’ merger. We find that for the mass parameters of $M\mu_S = 0.2, 0.4$, the oscillation frequencies are shifted to values larger than the mass parameter, $\omega_R > \mu_S$. For $M\mu_S = 0.6$, we see that the dominant oscillation frequency is determined by the mass parameter, $\omega_R = \mu_S$.

The scalar radiation excited by the BH binary with mass ratio $q = 1/2$, and the scalar’s frequency spectra are shown in Figs. 9 and 10. The scalar’s quadrupole, shown in the bottom panels of these figures, exhibits the same

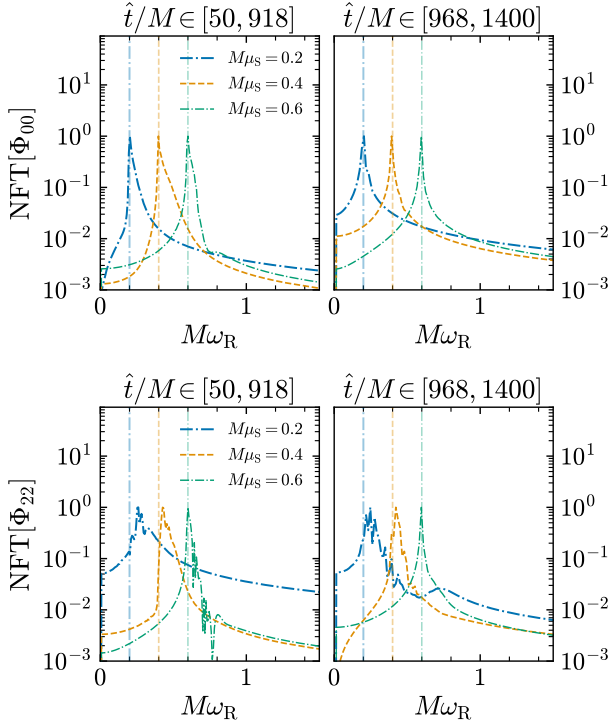


FIG. 8. Normalized Fourier transform of the scalar field $\ell = m = 0, 2$ multipoles extracted at $r_{\text{ex}} = 100M$ as function of the oscillation frequency for equal-mass binaries. We show the spectra before (left panels) and after the merger (right panels). The faded vertical lines indicate $\omega_R \sim \mu_S$.

features and dependencies on the mass parameters as for the equal-mass binary. Because of the BHs' unequal mass ratio, the scalar "charge" around each BH differs and, additionally, generates scalar dipole radiation shown in the middle panel of Fig. 9. For $M\mu_S = 0.2$, the dipole's amplitude remains approximately constant throughout the inspiral, and its frequency is slightly larger than the mass parameter, $\omega_R > \mu_S$. After the BHs have merged, the dipole's amplitude decays and its frequency is $\omega_R \simeq \mu_S$; see middle panel of Fig. 10. For larger mass parameters, $M\mu_S = 0.4, 0.6$, the amplitude of the dipole remains approximately constant throughout the binary's coalescence. Its frequency is determined by the mass parameters, $\omega_R \simeq \mu_S$, both before and after the merger.

The relative amount of scalar radiation for different scalar field mass parameters is related to the accretion onto the BHs. In the case of $M\mu_S = 0.2$, less of the scalar field is accreted onto the individual BHs, and it dissipates away from the binary. In turn, the amplitudes of the scalar's dipole and quadrupole drop during the first few orbits, and they remain approximately constant for the remainder of the inspiral. On the other hand, for the heavier scalar with $M\mu_S = 0.6$, there is stronger accretion and formation of scalar charges around the BHs. Consequently, the scalar dipole and quadrupole radiation remain nearly constant throughout the coalescence.

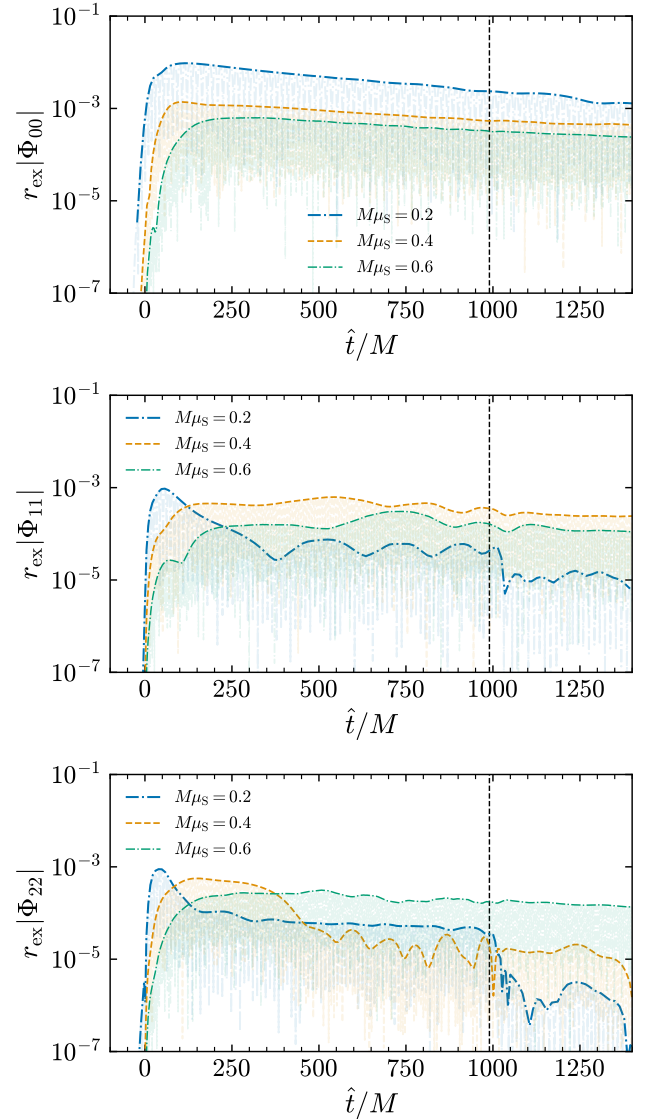


FIG. 9. Same as Fig. 7 but for binaries with $q = 1/2$. We show the scalar's $\ell = m = 0$ (top panel), $\ell = m = 1$ (middle panel) and $\ell = m = 2$ (bottom panel) multipoles.

D. Gravitational radiation

We now turn our attention to the gravitational radiation. In Figs. 11 and 12, we present the quadrupole of the Newman-Penrose scalar Ψ_4 (determining the outgoing gravitational radiation) for BH binaries with mass ratio $q = 1$ and $q = 1/2$, respectively. The gravitational waveforms are shifted in time by $r_{\text{ex}} = 100M$ to account for their propagation to the extraction sphere, and rescaled by the extraction radius to account for their $\sim 1/r$ fall-off. We present waveforms produced by a BH binary in vacuum and by binaries interacting with a scalar cloud of mass parameters $M\mu_S = \{0.2, 0.4, 0.6\}$. In all cases the gravitational radiation shows the familiar pattern of a sinusoid that is increasing in frequency and amplitude

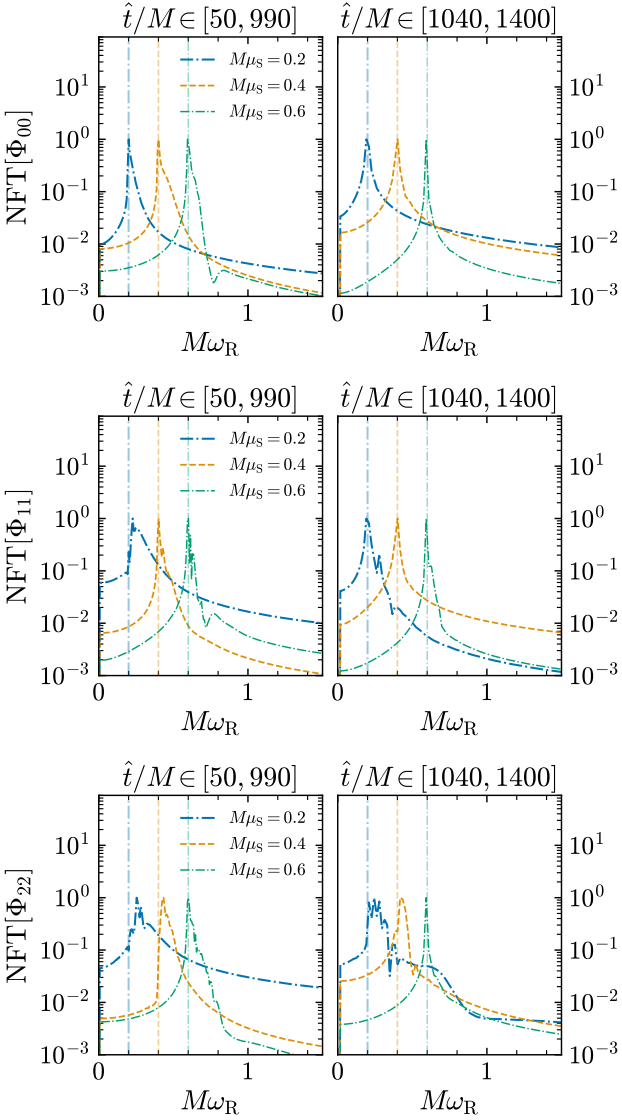


FIG. 10. Same as Fig. 8, but for binaries with $q = 1/2$. We show the normalized Fourier transforms of the scalar’s $\ell = m = 0$ (top panel), $\ell = m = 1$ (middle panel) and $\ell = m = 2$ (bottom panel) multipoles. The faded vertical lines indicate $\omega_R \sim \mu_S$.

during the inspiral until it peaks as the BHs merge, and is followed by the nearly monochromatic, exponentially decaying quasinormal mode ringdown.

As can be seen in the top panels of Figs. 11 and 12, the waveforms for different mass parameters agree in the early inspiral. This behaviour is consistent with the initial setup of a quasi-circular inspiral and comparable eccentricity of $\epsilon \lesssim 10^{-3}$ for all scalar mass parameters.

In the late inspiral we observe a dephasing shown more clearly in the middle panels of Figs. 11 and 12 where we display a zoom-in near the merger. The peak in the vacuum waveform is indicated by a vertical dashed line. In the case of equal-mass BH binaries displayed in Fig. 11,

we find that the peak in the waveform is shifted to earlier times for small scalar masses $M\mu_S = 0.2, 0.4$ while it is shifted to later times for the larger mass parameter $M\mu_S = 0.6$. We have verified that all phase shifts are larger than numerical error; see App. B. The former indicates an accelerated merger (time-to-merger) due to additional energy dissipated in scalar radiation. The latter indicates a delayed merger which we attribute to dynamical friction as the BHs sweep through the massive scalar cloud. For BH binaries with mass ratio $q = 1/2$, displayed in Fig. 12, we find that the peak in the waveform is shifted to later times for all scalar masses that we consider. We interpret the delayed merger as a consequence of dynamical friction which competes with an acceleration due to the scalar radiation.

The same trends in the phase shift are found in the $\ell = m = 3$ mode in the $q = 1/2$ simulations and in the $\ell = m = 4$ modes for both $q = 1$ and $q = 1/2$. In Fig. 13 below, we see that the phase shifts in the $\ell = m > 2$ modes are multiples of the shift in the $\ell = m = 2$ mode.

Our finding of an intricate dependency of the time-to-merger on the binary’s and scalar’s parameters is consistent with and complementary to those of Ref. [68], which report an accelerated merger for scalar mass parameters $M\mu_S \in \{0.0068, 0.86\}$. The authors focused on an equal-mass BH binary with a larger initial separation (and no eccentricity reduction) interacting with an initially homogeneous scalar field distribution of varying mass parameter. We find consistent results for simulations of equal-mass binaries with a scalar field of $M\mu_S = 0.2, 0.4$; see Fig. 11. We observe a delayed merger in particular for unequal-mass BH binaries that were not studied previously; see Fig. 12. Furthermore, we reduced the initial eccentricity to $\epsilon \lesssim 9 \times 10^{-3}$, whereas the simulations presented in Ref. [68] may contain some residual eccentricity. The latter typically accelerates the merger [120–122].

Finally, we analyse the quasinormal mode ringdown shown in the bottom panels of Figs. 11 and 12 for $q = 1$ and $q = 1/2$, respectively. To aid the visualization, we shift the waveforms such that their peaks are aligned. For both series of simulations, we find that the gravitational wave ringdown frequencies appear indistinguishable until about $\sim 100M$ after the merger. Only in the late stages of the ringdown ($\gtrsim 100M$) do we observe small differences in the quasinormal mode frequencies due to scalar cloud. This is consistent with results of Ref. [66], where the authors reported a small dependence of the gravitational wave ringdown frequency on the scalar’s mass parameter $M\mu_S$ that became observable only for scalar clouds whose density was three times larger than that of our simulations.

In the following subsection, we will discuss the dependence of physical observables on the properties of the scalar clouds in more detail.

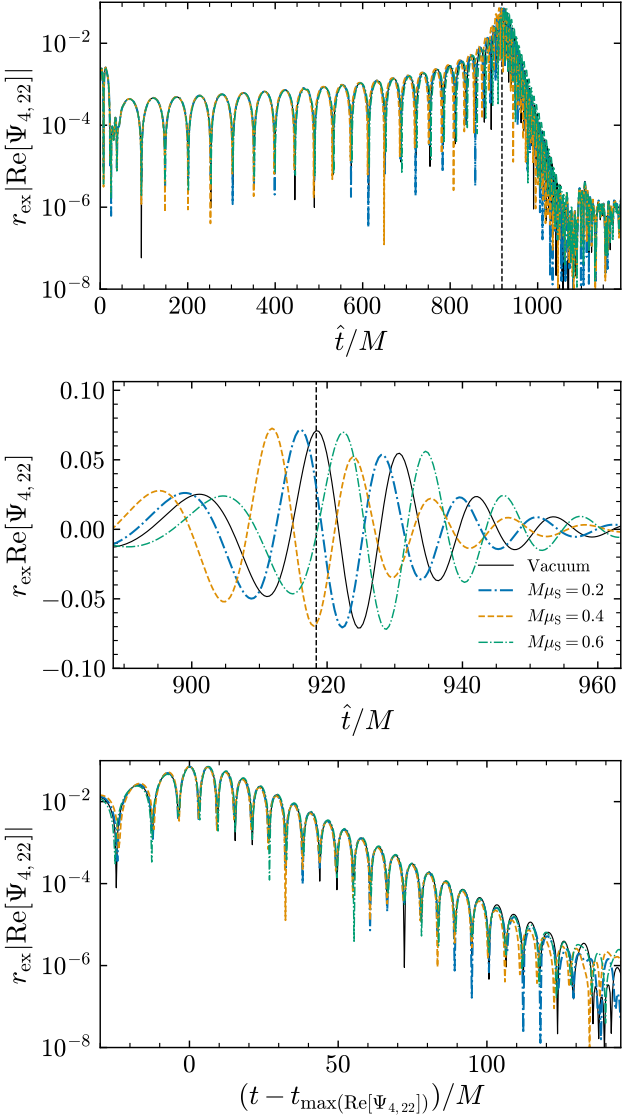


FIG. 11. Evolution of the real part of the quadrupole of the Newman-Penrose scalar, indicating outgoing gravitational radiation, for the equal-mass BH binary. We display the waveform for a binary in vacuum and binaries interacting with a scalar cloud of mass parameters $M\mu_S$. The waveforms in top and middle panels are shifted in time and rescaled by the extraction radius $r_{\text{ex}} = 100M$. The vertical dashed line indicates the peak in the waveform of the vacuum simulation. Top panel: complete waveform. Middle panel: zoom-in around the merger. Bottom panel: zoom-in of the quasinormal mode ringdown. Here, the time is shifted such that the peaks of the waveforms are aligned at $t - t_{\max(\text{Re}[\Psi_{4,22}])} = 0$.

E. Trends of physical observables

Here, we present the dependence of physical observables on all scalar field mass parameters $M\mu_S \in \{0.0, 0.2, \dots, 1.0\}$ considered in our simulation suites. The results are summarized in Fig. 13, where we show from top to bottom the gravitational wave phase shift

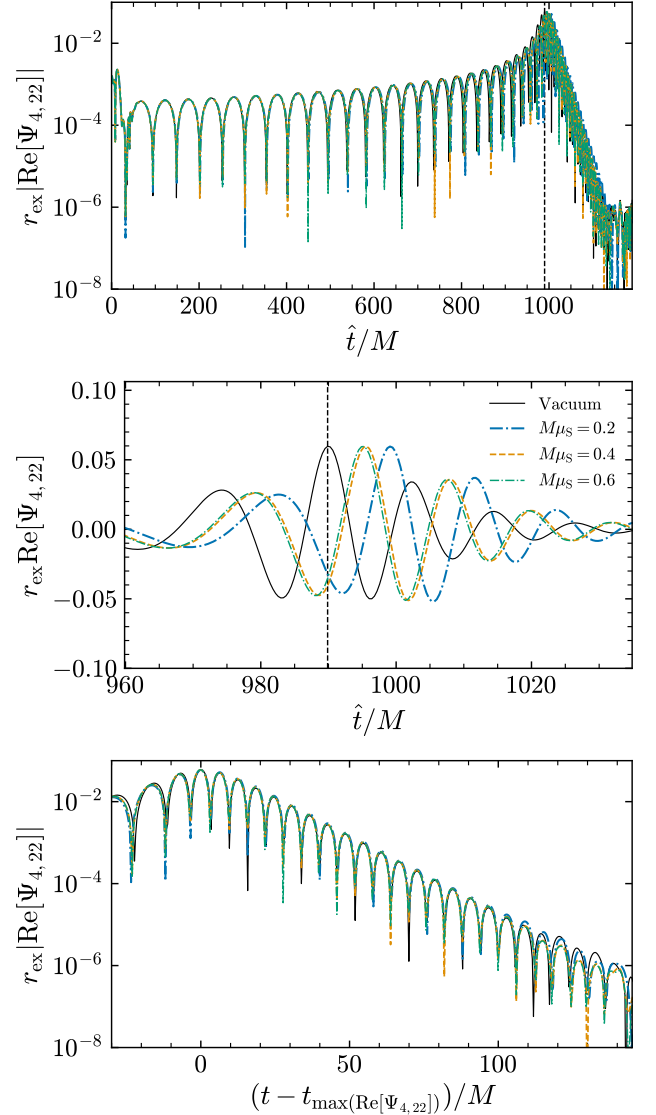


FIG. 12. Same as Fig. 11, but for a BH binary with mass ratio $q = 1/2$.

$\Delta\phi_{\ell m}$ in the $\ell = m = 2, 3, 4$ modes compared to the vacuum evolution, the peak frequency of the dominant gravitational waveform $\Psi_{4,22}$ extracted at $r_{\text{ex}} = 100M$, the peak luminosity of the gravitational radiation, and the total radiated energy in gravitational waves, E_{GW}/M .

The phase $\phi_{\ell m}$ of the (ℓ, m) mode of gravitational waveform is computed as a function of time by taking the complex argument of the Newman-Penrose scalar $\Psi_{4,\ell m}$. We quantify the GW phase shift as the difference between the GW phase in the presence of the scalar cloud and the phase in vacuum,

$$\Delta\phi_{\ell m} \equiv \phi_{\ell m} - \phi_{\ell m}^{\text{Vacuum}}. \quad (43)$$

We align the waveforms at $\hat{t} = t - r_{\text{ex}} = 100M$, after the initial junk radiation has passed. During the coalescence the magnitude of the phase difference accumulates and it

saturates after the BHs' merge. The phase shift reported in the top panel of Fig. 13 is computed after the saturation (corresponding to about $30M$ after the merger) when it has reached a constant value.

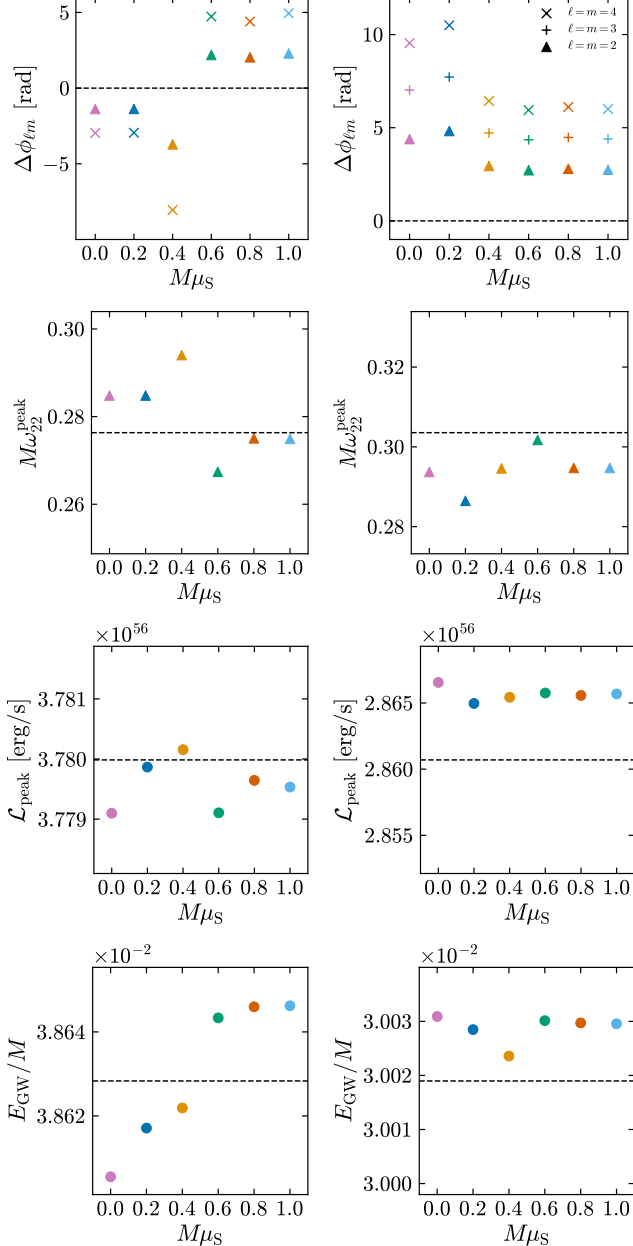


FIG. 13. Physical observables derived from Ψ_4 , extracted at $r_{\text{ex}} = 100M$, as a function of the scalar's mass parameter $M\mu_S$ for binaries with mass ratios $q = 1$ (left panels) and $q = 1/2$ (right panels). From top to bottom: GW phase shift $\Delta\phi_{\ell m}$ as compared to the vacuum waveform for the $\ell = m = 2, 3, 4$ multipoles; peak frequency $M\omega_{22}^{\text{peak}}$ of the GW quadrupole; peak luminosity $\mathcal{L}_{\text{peak}}$; and energy radiated in GWs, E_{GW}/M . The dashed horizontal lines denote the value of the observable in vacuum. The color coding of the symbols for each mass parameter is the same as in previous figures.

In the top panels of Fig. 13 we observe an intricate dependence of the GW phase on the scalar mass parameter and the BHs' mass ratio. In particular, in simulations of equal-mass binaries (top left panel), we find that the BHs' merger is accelerated with a peak (negative) phase shift for $M\mu_S = 0.4$. As the scalar's mass parameter is increased to $M\mu_S \geq 0.6$, we observe that the difference of the GW phase becomes positive, indicating a delayed merger, and this difference appears to saturate to a constant that is independent of the mass parameter. In simulations of BH binaries with mass ratio $q = 1/2$ shown in the top right panel of Fig. 13, we find a positive GW phase shift, indicating a delayed merger, for all scalar masses that we considered. The phase shift peaks around $M\mu_S = 0.2$ and then saturates to a constant value that seems to be independent of the scalar's mass. For the scalar cloud parameters considered in our simulations, the phase shift of the quadrupole, accumulated over seven orbits, can exceed half a GW cycle. We observe that the higher multipoles, $\ell = m = 3, 4$, also exhibit a GW phase shift. Their qualitative behaviour follows that of the quadrupole, but with a larger phase difference as shown in Fig. 13 that corresponds to 1.2 GW cycles for $\ell = m = 3$ and 1.7 GW cycles for $\ell = m = 4$.

Next, we compute the peak frequency of the GW quadrupole, $M\omega_{22}^{\text{peak}}$, as the maximum of the Fourier transformation of $\text{Re}[\Psi_{4,22}]$ taken in the time interval $\hat{t} \in (100M, \hat{t}_{\text{max}}(\text{Re}[\Psi_{4,22}]))$. The latter corresponds to the maximum of the time domain waveform, and so this interval captures the frequency evolution during the binaries' inspiral and merger. The result is shown in the second row of Fig. 13. In case of equal-mass binaries (left panel), we find a higher peak frequency than in vacuum for $M\mu_S \lesssim 0.4$, a lower frequency for $M\mu_S = 0.6$, and a value comparable to the vacuum one for $M\mu_S \gtrsim 0.8$. This dependency on the scalar's mass parameter is consistent with that of the GW phase shift. In case of the binaries with mass ratio $q = 1/2$ (right panel), we find a lower peak frequency for $M\mu_S \lesssim 0.2$, and a value comparable to the vacuum simulation for all $M\mu_S \gtrsim 0.4$. This trend is, again, consistent with the GW phase shift.

The previous discussion focuses on the frequency during the BHs' inspiral and merger. In the post-merger, the GW exhibits a quasinormal mode ringdown shown in the bottom panels of Figs. 11 and 12. We observe that the GW ringdown in the presence of the scalar field is essentially indistinguishable from that in vacuum. A frequency analysis indicates that the ringdown frequencies agree with those in vacuum within numerical error. This is due to the small density of the scalar cloud. To produce a difference of the ringdown frequency as reported in Ref. [66], it requires a density that is at least three times as large as the one we employ in our simulations.

We compute the GW luminosity, $\mathcal{L} \sim dE_{\text{GW}}/dt$, by integrating the Newman-Penrose scalar in time as defined in Eq. (24). In practice, we sum up to $\ell = 8$ multipoles, and perform the integration at $r_{\text{ex}} = 100M$. We display the maximum of the luminosity, $\mathcal{L}_{\text{peak}}$, in units of erg/s,

in the third row of Fig. 13. For both the equal-mass (left panel) and unequal-mass (right panel) binary we find that the peak luminosity is comparable to that in vacuum. We also observe that the luminosity appears to be independent of the scalar's mass parameter.

Finally, we obtain the total energy radiated in gravitational waves, E_{GW} , by integrating the luminosity in time. The result, in geometric units, is shown in the bottom panel of Fig. 13. As for the luminosity, we find that the radiated energy is largely independent of the scalar's mass parameter and that it differs from the vacuum case only at the sub-percent level.

In summary, we find that the GW phase and peak frequency depend on the scalar field's mass as well as the BHs' parameters (such as the mass ratio). In particular, we find an accelerated merger of equal-mass binaries that is most prominent for $M\mu_S = 0.4$, and a delayed merger for the unequal-mass binaries that is most prominent for $M\mu_S = 0.2$. For larger scalar field masses, the phase and frequency shifts seem to become insensitive to them.

There are several mechanisms that can introduce the GW dephasing in the presence of a scalar cloud. These include the growth of the BH through accretion of the scalar field, additional channels for energy loss through scalar radiation, and the formation of scalar wakes exerting a dynamical friction force on the BHs.

Let us consider the first mechanism: in Figs. 4 and 5 we see that the BHs accrete only a small amount of the scalar field during the inspiral, changing their masses by $\lesssim 0.04\%$. There is also no clear correspondence between the small increase in BH mass and the GW dephasing for the scalar configurations studied in this work.

Let us now consider the scalar radiation, discussed in Sec. V C. We find that energy is dissipated in the form of scalar waves with almost constant amplitude throughout the inspiral; see Figs. 7 and 9. The scalars' amplitude is comparable to that of the GWs in the early inspiral, and becomes subdominant in the late inspiral and merger. It may, thus, yield an acceleration of the inspiral.

Another contributor to accelerating the merger is the radial attraction between the BHs that results from the growth of a scalar overdensity in the binary's center of mass from an initially homogeneous distribution [68]. Such central overdensities appear small in our simulations which instead use an initial Gaussian profile; see the left panels in Fig. 3 and animations in Ref. [118].

Finally, let us turn to dynamical friction and drag forces that may cause an additional dephasing and, thus, compete with energy loss in scalar radiation. The drag forces depend on the BHs' speed as well as the scalar's mass parameter as was shown for single BHs in Refs. [43, 44], and, in the test field approximation, for BH binaries moving through a scalar wind in Ref. [45]. They also show that the drag force increases for large relative velocities between the BHs and scalar field. For the simulations presented here, using the coordinate data from PUNCTURETRACKER, we estimate that the BHs' average coordinate speed during the inspiral is $v \sim 0.15$ for

the equal-mass binary and $v \sim 0.1, 0.2$ for unequal-mass BHs with $q = 1/2$. Invoking the results of Refs. [43–45], we expect the drag forces to be small. It remains to be explored how such a formalism can be applied to fully nonlinear evolutions of the late inspiral, and if it may account for a delay of the merger. In summary, there is a clear understanding of an accelerated merger through scalar radiation, while the origin of the delayed mergers is not entirely clear. Longer simulations, left for future work, may reveal whether the acceleration becomes always dominant or if the delay becomes more prominent.

VI. CONCLUSIONS

In this work, we have investigated the impact of a massive scalar cloud, that may represent an overdense dark matter environment or a scalar condensate formed through superradiance, on coalescing BH binaries and their GW signal. We have performed fully general relativistic simulations that consistently include the interaction between the scalar field and the spacetime in the initial data, evolution and wave extraction. Complementary to existing initial data construction methods for the Einstein-Klein-Gordon system [67, 100, 123], we solve the constraints using the puncture approach. Therefore, we have extended the TwoPUNCTURES spectral solver [109] to include scalar condensates, and the resulting code TwoPUNCTURES_BBHSF [72] is open-source as a thorn of the EINSTEIN TOOLKIT [73, 74].

One of the goals of this work has been the implementation of software capable to produce high quality waveforms that include (dark matter) environmental effects on BH mergers and that are en par with numerical relativity waveform used in GW template building and data analysis. Therefore, we have extended our open-source software CANUDA by implementing up to eighth order finite difference stencils for spatial derivatives in the scalar and metric evolution thorns, and in the wave extraction.

We have also carefully reduced the initial orbital eccentricities below $\epsilon_\Omega \lesssim 9 \times 10^{-3}$ through an iterative procedure [110, 114]. Improving this procedure by extending post-Newtonian computations of binaries interacting with massive scalar fields [124] and extending numerical fitting procedures [119] would be valuable for extended simulation campaigns of quasi-circular BH binaries in such environments. Here, we have presented our upgraded software and a series of simulations geared towards high-quality waveform templates for next-generation gravitational wave detectors.

In this paper we presented two simulation series of binary BHs with mass ratios $q = 1, 1/2$. In each series, we systematically varied the scalar field's mass parameter in the range $M\mu_S \in \{0.0, 1.0\}$, while keeping the maximum of its initial (conformal) energy density approximately fixed at $\bar{\rho}_{\max} \approx 1.6 \times 10^{-7} M^{-2}$. While this value does represent a large dark matter overdensity, it is still physically viable; densities up to $\rho \sim 10^{-5} M^{-2}$ can be reached

by superradiant clouds [30] or dark matter surrounding an adiabatically growing BH [125]. This initial density, $\bar{\rho}_{\max} \approx 1.6 \times 10^{-7} M^{-2}$ in the geometric units of our simulations, corresponds to a density of $\rho \sim 10^{21} M_{\odot}/\text{pc}^3$ for a supermassive BH of $10^6 M_{\odot}$; c.f. Eq. (41).

Our simulations have shown that BH binaries surrounded by a scalar cloud, experience a dephasing. Specifically, we find both an accelerated and a delayed merger depending on the scalar's initial configuration and properties, and on the BHs' parameters. In the cases of $M\mu_S = 0.4$ for an equal-mass binary and $M\mu_S = 0.2$ for a binary with mass ratio $q = 1/2$, our simulations have shown that the GW phase shift of the dominant (quadrupole) mode induced by the scalar cloud can exceed half a GW cycle as compared to the merger in vacuum. Moreover, for $M\mu_S \gtrsim 0.5$, the observables seem to become insensitive to the mass parameter of the scalar. We find consistent trends in the peak frequency of the GW quadrupole, and in the phase shifts of the $\ell = m = 3, 4$ multipoles. In our analysis, we have examined the underlying mechanisms of scalar field accretion onto the BHs, scalar radiation, and drag forces which remain to be quantified in a fully nonlinear evolution.

A natural follow-up question to our study is whether the presence of a scalar cloud can be inferred from GW observables. Given the scalar cloud density considered in this work, we found that the main feature distinguishing the waveforms from the vacuum case is the GW dephasing and its shift in the peak frequency. These features appear consistently not only in the dominant GW quadrupole, but also in the higher multipoles. However, it is unclear whether the dephasing and frequency shift is unique to the presence of a massive scalar cloud, or if it can be degenerate with eccentric or spinning BH binaries that are known to introduce a phase shift [120, 122, 126].

Our work can be extended in several directions. To quantify potential degeneracies, it is crucial to compute the GW signature of spinning or eccentric BH binaries in a scalar cloud environment by extending proof-of-principle simulations [70], especially as new dynamical effects appear for spinning BHs [127, 128]. With our method of constructing initial data for non-homogeneous scalar clouds, it will be interesting to consider more realistic scalar field profiles representing dark matter halos or superradiant clouds. Our simulations also form the foundation for first mock parameter estimation studies to clarify if, and under which conditions, the presence of a scalar cloud may be detected in a GW signal. A very recent work in this direction can be found in Ref. [129].

Furthermore, the waveforms presented in this paper may inform tests of gravity and quantify potential degeneracies between modified gravity and environmental effects on GW waveforms. In particular, popular models of modified gravity such as scalar Gauss-Bonnet gravity or effective field theories of gravity yield a similar GW phase shift as observed here [130–132]. Whether or not GW signatures of modified gravity are degenerate with environmental effects on BH binaries is an open question.

VII. ACKNOWLEDGEMENTS

We thank J. Aurrekoetxea, J. Bamber, K. Clough, G. Pratten, P. Schmidt and H. O. Silva for insightful discussions and comments. The authors acknowledge support provided by the National Science Foundation under NSF Award No. OAC-2004879, No. PHY-2409726 and No. OAC-2411068. C.-H. C. acknowledges support provided by the Ministry of Education of Taiwan under the Taiwan-UIUC Scholarship. G. F. gratefully acknowledges the support of University of Calabria through a research fellowship funded by DR 1688/2023. We acknowledge the Texas Advanced Computing Center (TACC) at the University of Texas at Austin for providing HPC resources on Frontera via allocation PHY22041. This work used Delta CPU at NCSA through allocation PHY240117 from the Advanced Cyberinfrastructure Coordination Ecosystem: Services & Support (ACCESS) program, which is supported by U.S. National Science Foundation grants Nos. 2138259, 2138286, 2138307, 2137603, and 2138296. This research used resources provided by the Delta research computing project, which is supported by the NSF Award No. OAC-2005572 and the State of Illinois. This research was supported in part by the Illinois Computes project which is supported by the University of Illinois Urbana-Champaign and the University of Illinois System.

This work used the open-source softwares xTENSOR [133, 134], the EINSTEIN TOOLKIT [73, 74], CANUDA [76, 103], KUBIT [135], NUMPY [136], MATPLOTLIB [137], SCIPY [138], NRPy+ [111, 139].

The TwoPUNCTURES_BH_SF code developed to conduct this work is open source and available in the git repository [72]. A YouTube playlist with two-dimensional animations is available at Ref. [118].

Appendix A: BSSN formulation of the Einstein–Klein–Gordon equations

For completeness, we list the BSSN evolution equations as they are implemented in the CANUDALEANBSSNMOL and the SCALAROLVE thorns of the CANUDA code [76].

We evolve the spacetime using the W -version of the BSSN formulation [83]. Here, W refers to the conformal factor given by $W = \gamma^{-1/6}$, and γ is the determinant of the 3-metric. Other common choices for the conformal factor are χ or ϕ , which are related by $W^2 = \chi = e^{-4\phi}$ [84, 85]. The benefits of using W are (i) its avoidance of the $\mathcal{O}(\log r)$ singularity in ϕ at the puncture, and (ii) that the determinant of the 3-metric $\gamma = W^6$ remains positive.

The BSSN evolution variables are the conformal factor W and metric $\tilde{\gamma}_{ij}$, the trace K and (conformally rescaled) tracefree part \tilde{A}_{ij} of the extrinsic curvature and the con-

formal connection function $\tilde{\Gamma}^i$ defined as

$$W = \gamma^{-1/6}, \quad \tilde{\gamma}_{ij} = W^2 \gamma_{ij}, \quad (\text{A1a})$$

$$K = \gamma^{ij} K_{ij}, \quad \tilde{A}_{ij} = W^2 \left(K_{ij} - \frac{1}{3} \gamma_{ij} K \right), \quad (\text{A1b})$$

$$\tilde{\Gamma}^i = \tilde{\gamma}^{jk} \tilde{\Gamma}^i_{jk} = -\partial_j \tilde{\gamma}^{ij}. \quad (\text{A1c})$$

Here, $\tilde{\Gamma}^i_{jk}$ is the Christoffel connection of the conformal metric $\tilde{\gamma}_{ij}$ and the last relation holds because $\det \tilde{\gamma}_{ij} = 1$.

The time evolution of the BSSN variables is determined by a set of coupled, partial differential equations. For completeness, we provide the evolution equations as they are implemented in CANUDA_LEANBSSNMOL,

$$\partial_t W = \beta^i \partial_i W - \frac{1}{3} W \partial_i \beta^i + \frac{1}{3} \alpha W K, \quad (\text{A2a})$$

$$\begin{aligned} \partial_t \tilde{\gamma}_{ij} &= \beta^k \partial_k \tilde{\gamma}_{ij} + \tilde{\gamma}_{ik} \partial_j \beta^k + \tilde{\gamma}_{jk} \partial_i \beta^k - \frac{2}{3} \tilde{\gamma}_{ij} \partial_k \beta^k \\ &\quad - 2\alpha \tilde{A}_{ij}, \end{aligned} \quad (\text{A2b})$$

$$\begin{aligned} \partial_t K &= \beta^k \partial_k K - \gamma^{ij} D_i D_j \alpha \\ &\quad + \alpha \left[\tilde{A}^{ij} \tilde{A}_{ij} + \frac{1}{3} K^2 + 4\pi(\rho + S) \right], \end{aligned} \quad (\text{A2c})$$

$$\begin{aligned} \partial_t \tilde{A}_{ij} &= \beta^k \partial_k \tilde{A}_{ij} + \tilde{A}_{ik} \partial_j \beta^k + \tilde{A}_{jk} \partial_i \beta^k - \frac{2}{3} \tilde{A}_{ij} \partial_k \beta^k \\ &\quad + W^2 [\alpha R_{ij} - D_i D_j \alpha]^{\text{TF}} + \alpha \left(K \tilde{A}_{ij} - 2\tilde{A}_i{}^k \tilde{A}_{jk} \right) \\ &\quad - 8\pi\alpha W^2 [S_{ij}]^{\text{TF}}, \end{aligned} \quad (\text{A2d})$$

$$\begin{aligned} \partial_t \tilde{\Gamma}^i &= \beta^k \partial_k \tilde{\Gamma}^i + \frac{2}{3} \tilde{\Gamma}^i \partial_k \beta^k - \tilde{\Gamma}^k \partial_k \beta^i \\ &\quad - \frac{4}{3} \alpha \tilde{\gamma}^{ik} \tilde{D}_k K + \frac{1}{3} \tilde{\gamma}^{ik} \partial_k \partial_j \beta^j + \tilde{\gamma}^{kj} \partial_j \partial_k \beta^i \\ &\quad - 2\alpha \tilde{\Gamma}_{jk}^i \tilde{A}^{jk} - 2\tilde{A}^{ik} \left(\tilde{D}_k \alpha + 3\alpha \frac{\tilde{D}_k W}{W} \right) - 16\pi\alpha j^i \\ &\quad - \left(\sigma + \frac{2}{3} \right) \left(\tilde{\Gamma}^i - \tilde{\gamma}^{jk} \tilde{\Gamma}^i_{jk} \right) \partial_l \beta^l. \end{aligned} \quad (\text{A2e})$$

Here, \tilde{D}_i indicates the covariant derivative associated with the conformal metric $\tilde{\gamma}_{ij}$, $[\dots]^{\text{TF}}$ denotes the trace-free part, and we use as short-hand notation

$$\begin{aligned} D_i D_j \alpha &= \frac{1}{W} \left(\tilde{D}_i \alpha \tilde{D}_j W + \tilde{D}_j \alpha \tilde{D}_i W - \tilde{\gamma}_{ij} \tilde{D}^k \alpha \tilde{D}_k W \right) \\ &\quad + \tilde{D}_i \tilde{D}_j \alpha, \end{aligned} \quad (\text{A3a})$$

$$\begin{aligned} R_{ij} &= \tilde{R}_{ij} + \frac{1}{W} \left(\tilde{D}_i \tilde{D}_j W + \tilde{\gamma}_{ij} \tilde{D}^k \tilde{D}_k W \right) \\ &\quad - \frac{2}{W^2} \tilde{\gamma}_{ij} \tilde{D}^k W \tilde{D}_k W. \end{aligned} \quad (\text{A3b})$$

The energy density ρ , energy-momentum flux j_i , and stress tensor S_{ij} are read in from the TMUNUBASE thorn.

During the numerical evolution, we enforce the algebraic constraints that \tilde{A}_{ij} is trace-free, i.e., $\tilde{\gamma}^{ij} \tilde{A}_{ij} = 0$.

The definition of the conformal connection function in Eq. (A1c) implies a differential constraint. As in

the LEAN code [89], we augment the evolution equation of the conformal connection function with a term $\sim (\tilde{\Gamma}^i - \tilde{\gamma}^{jk} \tilde{\Gamma}^i_{jk})$ in Eq. (A2e). This modification was introduced by Yo et al [140] to mitigate the growth of any numerical error in $\tilde{\Gamma}^i$ which could result in numerical instabilities. This extra term vanishes in the continuum limit by construction of $\tilde{\Gamma}^i$. We typically set the free parameter $\sigma = 0$ by default.

The spacetime evolution equations are closed by the moving puncture gauge for the lapse function and shift vector [84, 85, 87], in the form given in Eq. (15).

The scalar field's evolution equations are implemented in CANUDA's SCALAR-EVOLVE thorn using the BSSN variables. Their explicit form is given by

$$\partial_t \Phi = -2\alpha \Pi + \beta^k \tilde{D}_k \Phi, \quad (\text{A4a})$$

$$\begin{aligned} \partial_t \Pi &= \frac{\alpha}{2} \left(-W^2 \tilde{D}^k \tilde{D}_k \Phi + \tilde{D}^k \Phi \tilde{D}_k W + 2K\Pi + \mu_S^2 \Phi \right) \\ &\quad + \beta^k \tilde{D}_k \Pi - \frac{1}{2} W^2 \tilde{D}^i \alpha \tilde{D}_i \Phi. \end{aligned} \quad (\text{A4b})$$

Appendix B: Convergence test and error estimate

We perform convergence tests to verify that the simulations are run at a sufficiently high resolution to be in the convergent regime, and to assess their numerical error. Therefore, we run simulations at three different spatial resolutions $\Delta x_f < \Delta x_m < \Delta x_c$, and compute the residuals of a quantity h between the fine and medium resolution results $|h_f - h_m|$, and the medium and coarse resolution results $|h_m - h_c|$. If these results are convergent at n -th order, then the residuals are proportional to the numerical error and satisfy [88]

$$\frac{|h_m - h_c|}{|h_f - h_m|} = Q_n \equiv \frac{\Delta x_m^n - \Delta x_c^n}{\Delta x_f^n - \Delta x_m^n}, \quad (\text{B1})$$

where Q_n is the n -th order convergence factor for the resolutions considered.

We perform the convergence analysis using the most demanding simulation setup, **q12mu04** in Table I, i.e., a binary BH with mass ratio $q = 1/2$ and a scalar field with mass parameter $M\mu_S = 0.4$. We run setup **q12mu04** at three different resolutions $\Delta x_f = 0.729$, $\Delta x_m = 0.81$, $\Delta x_c = 0.854$ defined on the outermost refinement level, and examine if the criterion in Eq. (B1) is satisfied. The corresponding convergence factors are $Q_4 = 0.685$, $Q_6 = 0.797$, and $Q_8 = 0.925$ for fourth, sixth and eighth order convergence, respectively. In all production simulations, we employed eighth order finite difference stencils for spatial derivatives of the metric, scalar field and for the Newman-Penrose scalars. The time integration employs a fourth order Runge-Kutta integrator, while the interpolator at refinement boundaries is of second order in time and fifth order in space. Therefore, we may expect a mixed convergence order in our simulations.

In Fig. 14, we present the convergence test of the real part of the $(\ell, m) = (2, 2)$ mode of the Newman-Penrose scalar Ψ_4 extracted on coordinate spheres of radius $r_{\text{ex}} = 100M$. We find that the waveforms are eighth order convergent in the early part of the simulation before $\hat{t} \lesssim 600M$, over-convergent during the merger and ringdown $\hat{t} \gtrsim 900M$, until the waves amplitude becomes comparable to numerical noise at $\hat{t} \gtrsim 1100M$. However, the convergence order drops below fourth order in the interval $600M \lesssim \hat{t} \lesssim 900M$ right before the merger. This is likely due to the different discretization orders used in spatial derivatives, time integrator and interpolator as outlined above.

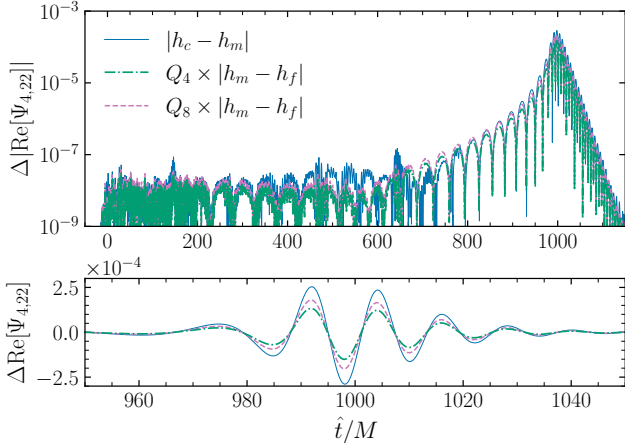


FIG. 14. Convergence plot for the evolution of the quadrupole gravitational wave mode, $h = \text{Re}[\Psi_{4,22}]$, extracted at $r_{\text{ex}} = 100M$. We plot the residual $|h_f - h_m|$ between the fine ($\Delta x_f = 0.729$) and medium resolution ($\Delta x_m = 0.81$) simulations, and the residual $|h_m - h_c|$ between the medium and coarse resolution ($\Delta x_c = 0.854$) simulations multiplied by the convergence factors Q_4 and Q_8 . The bottom panel displays a zoom in around the merger.

The simulations presented in this paper have been produced with the coarse resolution ($\Delta x_c = 0.854$) run. Having determined the convergence order of the waveform, we now estimate the relative error of the coarse resolution run with respect to (i) the finest resolution ($\Delta x_f = 0.729$), and (ii) the fourth and eighth order Richardson extrapolation of the waveform as benchmark.

More precisely, the n -th order Richardson extrapolation, h_{On} , using the fine and coarse numerical solutions h_c and h_f is obtained from [88]

$$h_{On} = h_f - \frac{1}{(\Delta x_c/\Delta x_f)^n - 1} (h_c - h_f) + \mathcal{O}(\Delta x_f^{n+1}), \quad (\text{B2})$$

where $\Delta x_c/\Delta x_f = 0.854/0.729$. The extrapolated solution in Eq. (B2) is accurate to order $n + 1$ in the spatial resolution if the numerical solutions are in the convergent regime. Having verified that the gravitational waveform are sixth to eighth order convergent, we can employ the

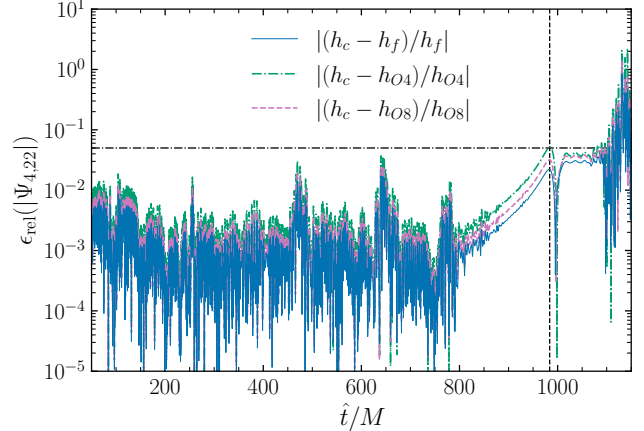


FIG. 15. Relative error of $|\Psi_{4,22}|$, computed by the coarse resolution simulation and compared to the fine resolution simulation, the fourth and eighth order Richardson extrapolated waveforms as reference solutions. The black horizontal dotted-dashed line indicates a relative error of 5%, and the black vertical dashed line indicates the merger time determined by the formation of the common apparent horizon.

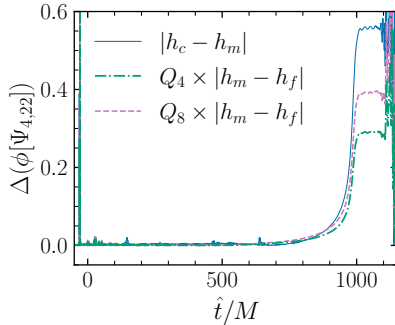


FIG. 16. Convergence plot for the complex phase $h = \phi[\Psi_{4,22}]$ using the waveform extracted at $r_{\text{ex}} = 100M$. The phase is measured from the time $t - r_{\text{ex}} = 100M$ to define the zero point of the phase. We plot the residual $h_f - h_m$ between the fine ($\Delta x_f = 0.729$) and medium resolution ($\Delta x_m = 0.81$) simulations, and the residual $h_m - h_c$ between the medium and coarse resolution ($\Delta x_c = 0.854$) simulations scaled by the convergence factors Q_6 and Q_8 .

Richardson extrapolated solution as benchmark for the error analysis.

Next, we estimate the relative error

$$\epsilon_{\text{rel}} = \left| \frac{(h - h_{\text{reference}})}{h_{\text{reference}}} \right|, \quad (\text{B3})$$

of a function h at a given resolution compared to the reference solution of that function. In the following, we compute the relative error using as reference solution the fine resolution data, and the fourth or eighth order Richardson extrapolated quantities. We plot the relative errors of the modulus of $\Psi_{4,22}$ in Fig. 15, and find that it is below $\sim 1\%$ throughout the early inspiral ($\hat{t} \lesssim 900M$),

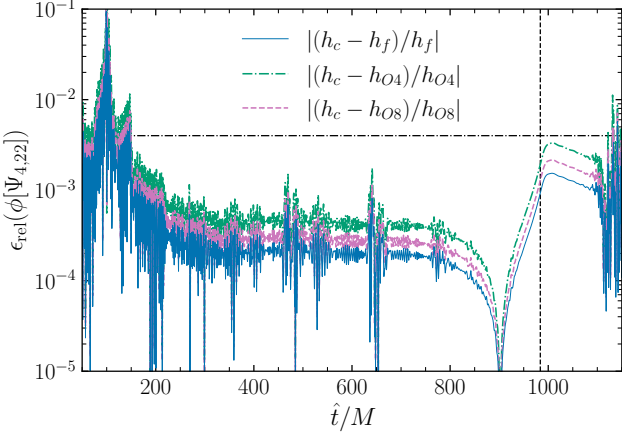


FIG. 17. Same as Fig. 15 but for the phase of $\Psi_{4,22}$. The black horizontal dotted-dashed line indicates a relative error of 0.4%, and the black vertical dashed line indicates the merger time.

and below $\sim 4\%$ in the late inspiral, merger and ringdown ($900M \lesssim \hat{t} \lesssim 1100M$). The relative error increases after the ringdown when the waveform has such a small amplitude that it is dominated by numerical noise.

Next, we test the convergence of the phase of the $(\ell, m) = (2, 2)$ mode of Ψ_4 extracted on $r_{\text{ex}} = 100M$. The phase is computed by measuring the complex argument of $\Psi_{4,22}$ with respect to a starting point, which we choose to be $\hat{t} = 100M$, corresponding to the first cycle in the gravitational wave. The result is shown in Fig. 16. Similar to the real part of the Newman-Penrose scalar (c.f. Fig. 14), we find eighth order convergence in the early inspiral ($\hat{t} \lesssim 600M$), fourth order convergence in the late inspiral ($600M \lesssim \hat{t} \lesssim 900M$), and overconvergence in the merger and ringdown ($\hat{t} \gtrsim 900M$).

We compute the fourth and eighth order Richardson extrapolation of the phase $h = \phi[\Psi_{4,22}]$. We calculate the relative error of the coarse resolution simulation using the fine resolution data h_f and the Richardson extrapolated data. In Fig. 17 we show that the relative error in the phase stays below 1% percent for the duration of the simulation until the end of the ringdown at $t - r_{\text{ex}} = 1100M$, where the waveforms are dominated by numerical noise.

Finally, in Figs. 18 and 19 we present the relative error of the Christodoulou masses of the individual and final BHs, and the dimensionless spin of the final BH, extracted by QUASILOCALMEASURES. These quantities are defined in Eqs. (38) and (39), and we only show the comparison between low- and high-resolution data. Prior to the merger, the Christodoulou mass of each BH has relative error $\epsilon_{\text{rel}}(M_{(a)}) \lesssim 10^{-5}$. After the merger, the final BH has a relative error of $\epsilon_{\text{rel}}(M_f) \lesssim 2 \times 10^{-6}$.

The final BH acquires a dimensionless spin of $\chi_f \sim 0.62$ after the merger. Its relative error is $\epsilon_{\text{rel}}(\chi_f) \lesssim 10^{-4}$, which stays approximately constant throughout the ringdown.

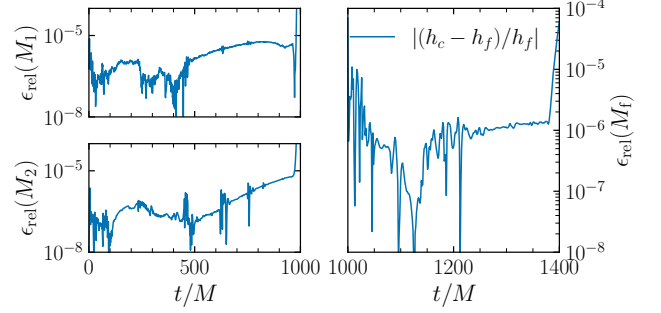


FIG. 18. Relative error of the Christodoulou mass of the individual BHs before the merger (left panels) and the final BH (right panel).

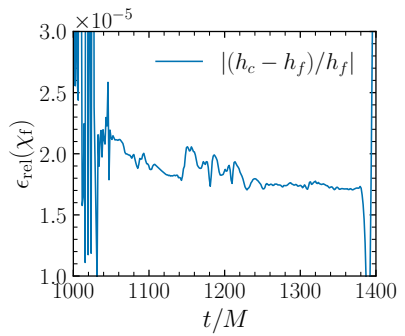


FIG. 19. Relative error of the dimensionless spin $\chi_f \equiv J_f/M_f^2$ of the final BH.

-
- [1] B. P. Abbott *et al.* (LIGO Scientific, Virgo), *Phys. Rev. Lett.* **116**, 061102 (2016), arXiv:1602.03837 [gr-qc].
- [2] A. G. Abac *et al.* (LIGO Scientific, VIRGO, KAGRA), GWTC-4.0: Updating the Gravitational-Wave Transient Catalog with Observations from the First Part of the Fourth LIGO-Virgo-KAGRA Observing Run (2025), arXiv:2508.18082 [gr-qc].
- [3] M. Maggiore *et al.* (ET), *JCAP* **03**, 050, arXiv:1912.02622 [astro-ph.CO].
- [4] D. Reitze *et al.*, Bull. Am. Astron. Soc. **51**, 035 (2019), arXiv:1907.04833 [astro-ph.IM].
- [5] K. G. Arun *et al.* (LISA), *Living Rev. Rel.* **25**, 4 (2022), arXiv:2205.01597 [gr-qc].
- [6] L. Hui, J. P. Ostriker, S. Tremaine, and E. Witten, *Phys. Rev. D* **95**, 043541 (2017), arXiv:1610.08297 [astro-ph.CO].
- [7] S. R. Dolan, *Phys. Rev. D* **76**, 084001 (2007), arXiv:0705.2880 [gr-qc].
- [8] D. Baumann, H. S. Chia, J. Stout, and L. ter Haar, *JCAP* **12**, 006, arXiv:1908.10370 [gr-qc].
- [9] M. Pato, F. Iocco, and G. Bertone, *JCAP* **12**, 001, arXiv:1504.06324 [astro-ph.GA].
- [10] G. D. Quinlan, L. Hernquist, and S. Sigurdsson, *Astrophys. J.* **440**, 554 (1995), arXiv:astro-ph/9407005.
- [11] P. Gondolo and J. Silk, *Phys. Rev. Lett.* **83**, 1719 (1999), arXiv:astro-ph/9906391.
- [12] P. Ullio, H. Zhao, and M. Kamionkowski, *Phys. Rev. D* **64**, 043504 (2001), arXiv:astro-ph/0101481.
- [13] B. J. Kavanagh, D. A. Nichols, G. Bertone, and D. Gaggero, *Phys. Rev. D* **102**, 083006 (2020), arXiv:2002.12811 [gr-qc].
- [14] A. Coogan, G. Bertone, D. Gaggero, B. J. Kavanagh, and D. A. Nichols, *Phys. Rev. D* **105**, 043009 (2022), arXiv:2108.04154 [gr-qc].
- [15] H. Kim, A. Lenoci, I. Stomberg, and X. Xue, *Phys. Rev. D* **107**, 083005 (2023), arXiv:2212.07528 [astro-ph.GA].
- [16] L. Hui, D. Kabat, X. Li, L. Santoni, and S. S. C. Wong, *JCAP* **06**, 038, arXiv:1904.12803 [gr-qc].
- [17] F. Hancock and H. Witek, *Phys. Rev. D* **112**, 044033 (2025), arXiv:2506.06554 [gr-qc].
- [18] K. Clough, P. G. Ferreira, and M. Lagos, *Phys. Rev. D* **100**, 063014 (2019), arXiv:1904.12783 [gr-qc].
- [19] J. Bamber, K. Clough, P. G. Ferreira, L. Hui, and M. Lagos, *Phys. Rev. D* **103**, 044059 (2021), arXiv:2011.07870 [gr-qc].
- [20] R. Brito, V. Cardoso, and P. Pani, *Lect. Notes Phys.* **906**, pp.1 (2015), arXiv:1501.06570 [gr-qc].
- [21] S. L. Detweiler, *Phys. Rev. D* **22**, 2323 (1980).
- [22] H. Witek, V. Cardoso, A. Ishibashi, and U. Sperhake, *Phys. Rev. D* **87**, 043513 (2013), arXiv:1212.0551 [gr-qc].
- [23] Y. Shlapentokh-Rothman, *Commun. Math. Phys.* **329**, 859 (2014), arXiv:1302.3448 [gr-qc].
- [24] W. E. East and F. Pretorius, *Phys. Rev. Lett.* **119**, 041101 (2017), arXiv:1704.04791 [gr-qc].
- [25] W. E. East and N. Siemonsen, *Phys. Rev. D* **108**, 124048 (2023), arXiv:2309.05096 [gr-qc].
- [26] C. A. R. Herdeiro and E. Radu, *Phys. Rev. Lett.* **112**, 221101 (2014), arXiv:1403.2757 [gr-qc].
- [27] J. Nicoules, J. Ferreira, C. A. R. Herdeiro, E. Radu, and M. Zilhão, Splitting the Gravitational Atom: Instabilities of Black Holes with Synchronized/Resonant Hair (2025), arXiv:2509.20450 [gr-qc].
- [28] R. Brito, V. Cardoso, and P. Pani, *Class. Quant. Grav.* **32**, 134001 (2015), arXiv:1411.0686 [gr-qc].
- [29] G. Ficarra, P. Pani, and H. Witek, *Phys. Rev. D* **99**, 104019 (2019), arXiv:1812.02758 [gr-qc].
- [30] L. Hui, Y. T. A. Law, L. Santoni, G. Sun, G. M. Tomaselli, and E. Trincherini, *Phys. Rev. D* **107**, 104018 (2023), arXiv:2208.06408 [gr-qc].
- [31] C. F. B. Macedo, P. Pani, V. Cardoso, and L. C. B. Crispino, *Astrophys. J.* **774**, 48 (2013), arXiv:1302.2646 [gr-qc].
- [32] R. Brito, S. Ghosh, E. Barausse, E. Berti, V. Cardoso, I. Dvorkin, A. Klein, and P. Pani, *Phys. Rev. D* **96**, 064050 (2017), arXiv:1706.06311 [gr-qc].
- [33] S. Ghosh, E. Berti, R. Brito, and M. Richartz, *Phys. Rev. D* **99**, 104030 (2019), arXiv:1812.01620 [gr-qc].
- [34] J. Zhang and H. Yang, *Phys. Rev. D* **101**, 043020 (2020), arXiv:1907.13582 [gr-qc].
- [35] N. Siemonsen, T. May, and W. E. East, *Phys. Rev. D* **107**, 104003 (2023), arXiv:2211.03845 [gr-qc].
- [36] E. Barausse, V. Cardoso, and P. Pani, *Phys. Rev. D* **89**, 104059 (2014), arXiv:1404.7149 [gr-qc].
- [37] D. Baumann, H. S. Chia, and R. A. Porto, *Phys. Rev. D* **99**, 044001 (2019), arXiv:1804.03208 [gr-qc].
- [38] D. Baumann, G. Bertone, J. Stout, and G. M. Tomaselli, *Phys. Rev. Lett.* **128**, 221102 (2022), arXiv:2206.01212 [gr-qc].
- [39] G. M. Tomaselli, T. F. M. Spieksma, and G. Bertone, *Phys. Rev. Lett.* **133**, 121402 (2024), arXiv:2407.12908 [gr-qc].
- [40] M. Bošković, M. Koschnitzke, and R. A. Porto, *Phys. Rev. Lett.* **133**, 121401 (2024), arXiv:2403.02415 [gr-qc].
- [41] Q. Yang, L.-W. Ji, B. Hu, Z.-J. Cao, and R.-G. Cai, *Res. Astron. Astrophys.* **18**, 065 (2018), arXiv:1706.00678 [gr-qc].
- [42] D. Traykova, K. Clough, T. Helfer, E. Berti, P. G. Ferreira, and L. Hui, *Phys. Rev. D* **104**, 103014 (2021), arXiv:2106.08280 [gr-qc].
- [43] R. Vicente and V. Cardoso, Dynamical friction of black holes in ultralight dark matter (2022), arXiv:2201.08854 [gr-qc].
- [44] D. Traykova, R. Vicente, K. Clough, T. Helfer, E. Berti, P. G. Ferreira, and L. Hui, *Phys. Rev. D* **108**, L121502 (2023), arXiv:2305.10492 [gr-qc].
- [45] S. Xin and E. R. Most, Relativistic scalar dark matter drag forces on a black hole binary (2025), arXiv:2507.18934 [gr-qc].
- [46] J. Zhang and H. Yang, *Phys. Rev. D* **99**, 064018 (2019), arXiv:1808.02905 [gr-qc].
- [47] V. Cardoso, F. Duque, and T. Ikeda, *Phys. Rev. D* **101**, 064054 (2020), arXiv:2001.01729 [gr-qc].
- [48] T. Takahashi and T. Tanaka, *JCAP* **10**, 031, arXiv:2106.08836 [gr-qc].
- [49] L. Annuluri, V. Cardoso, and R. Vicente, *Phys. Lett. B* **811**, 135944 (2020), arXiv:2007.03700 [astro-ph.HE].
- [50] L. Annuluri, V. Cardoso, and R. Vicente, *Phys. Rev. D* **102**, 063022 (2020), arXiv:2009.00012 [gr-qc].
- [51] T. Takahashi, H. Omiya, and T. Tanaka, *Phys. Rev. D* **110**, 104038 (2024), arXiv:2408.08349 [gr-qc].
- [52] A. Maselli, N. Franchini, L. Gualtieri, and T. P.

- Sotiriou, *Phys. Rev. Lett.* **125**, 141101 (2020), arXiv:2004.11895 [gr-qc].
- [53] A. Maselli, N. Franchini, L. Gualtieri, T. P. Sotiriou, S. Barsanti, and P. Pani, *Nature Astron.* **6**, 464 (2022), arXiv:2106.11325 [gr-qc].
- [54] S. Barsanti, A. Maselli, T. P. Sotiriou, and L. Gualtieri, *Phys. Rev. Lett.* **131**, 051401 (2023), arXiv:2212.03888 [gr-qc].
- [55] S. Barsanti, N. Franchini, L. Gualtieri, A. Maselli, and T. P. Sotiriou, *Phys. Rev. D* **106**, 044029 (2022), arXiv:2203.05003 [gr-qc].
- [56] V. Cardoso, K. Destounis, F. Duque, R. Panosso Macedo, and A. Maselli, *Phys. Rev. Lett.* **129**, 241103 (2022), arXiv:2210.01133 [gr-qc].
- [57] F. Duque, C. F. B. Macedo, R. Vicente, and V. Cardoso, *Phys. Rev. Lett.* **133**, 121404 (2024), arXiv:2312.06767 [gr-qc].
- [58] R. Brito and S. Shah, *Phys. Rev. D* **108**, 084019 (2023), [Erratum: *Phys. Rev. D* 110, 109902 (2024)], arXiv:2307.16093 [gr-qc].
- [59] M. Della Rocca, S. Barsanti, L. Gualtieri, and A. Maselli, *Phys. Rev. D* **109**, 104079 (2024), arXiv:2401.09542 [gr-qc].
- [60] C. Dyson, T. F. M. Spieksma, R. Brito, M. van de Meent, and S. Dolan, Environmental effects in extreme mass ratio inspirals: perturbations to the environment in Kerr (2025), arXiv:2501.09806 [gr-qc].
- [61] P. S. Cole, G. Bertone, A. Coogan, D. Gaggero, T. Karydas, B. J. Kavanagh, T. F. M. Spieksma, and G. M. Tomaselli, *Nature Astron.* **7**, 943 (2023), arXiv:2211.01362 [gr-qc].
- [62] X.-J. Yue, W.-B. Han, and X. Chen, *Astrophys. J.* **874**, 34 (2019), arXiv:1802.03739 [gr-qc].
- [63] E. Berti, R. Brito, C. F. B. Macedo, G. Raposo, and J. L. Rosa, *Phys. Rev. D* **99**, 104039 (2019), arXiv:1904.03131 [gr-qc].
- [64] A. Guo, J. Zhang, and H. Yang, *Phys. Rev. D* **110**, 023022 (2024), arXiv:2401.15003 [gr-qc].
- [65] A. Guo, Q.-Y. Zhang, H. Yang, and J. Zhang, Common Envelope Evolution of Ultralight Boson Clouds (2025), arXiv:2508.18738 [gr-qc].
- [66] S. Choudhary, N. Sanchis-Gual, A. Gupta, J. C. Degollado, S. Bose, and J. A. Font, *Phys. Rev. D* **103**, 044032 (2021), arXiv:2010.00935 [gr-qc].
- [67] J. C. Aurrekoetxea, K. Clough, and E. A. Lim, *Class. Quant. Grav.* **40**, 075003 (2023), arXiv:2207.03125 [gr-qc].
- [68] J. C. Aurrekoetxea, K. Clough, J. Bamber, and P. G. Ferreira, *Phys. Rev. Lett.* **132**, 211401 (2024), arXiv:2311.18156 [gr-qc].
- [69] J. C. Aurrekoetxea, J. Marsden, K. Clough, and P. G. Ferreira, *Phys. Rev. D* (2024), arXiv:2409.01937 [gr-qc].
- [70] Y.-P. Zhang, M. Gracia-Linares, P. Laguna, D. Shoemaker, and Y.-X. Liu, *Phys. Rev. D* **107**, 044039 (2023), arXiv:2209.11814 [gr-qc].
- [71] S. Brandt and B. Bruegmann, *Phys. Rev. Lett.* **78**, 3606 (1997), arXiv:gr-qc/9703066.
- [72] Canuda: TwoPunctures_BBHSF: Git Repository (2024).
- [73] The Einstein Toolkit: Website.
- [74] R. Haas, M. Rizzo, D. Boyer, S. R. Brandt, P. Diener, D. Garzon, L. T. Sanches, B.-J. Tsao, S. Cupp, Z. Etienne, T. P. Jacques, L. Ji, E. Schnetter, L. Werneck, M. Alcubierre, D. Alic, G. Allen, M. Ansorg, F. G. L. Armengol, M. Babiu-Hamilton, L. Baiotti, W. Benger, E. Bentivegna, S. Bernuzzi, K. Bhatia, T. Bode, G. Bozzola, B. Brendal, B. Bruegmann, M. Campanelli, M. Chabanov, C.-H. Cheng, F. Cipolletta, G. Corvino, R. D. Pietri, A. Dima, H. Dimmelmeier, J. Doherty, R. Dooley, N. Dorband, M. Elley, Y. E. Khamra, L. Ennoggi, J. Faber, G. Ficarra, T. Font, J. Frieben, B. Giacomazzo, T. Goodale, C. Gundlach, I. Hawke, S. Hawley, I. Hinder, E. A. Huerta, S. Husa, T. Ikeda, S. Iyer, D. Johnson, A. V. Joshi, J. Kalinani, A. Kankani, W. Kastaun, T. Kellermann, A. Knapp, M. Koppitz, P. Laguna, G. Lanferman, P. Lasky, F. Löffler, H. Macpherson, I. Markin, J. Masso, L. Menger, A. Merzky, J. M. Miller, M. Miller, P. Moesta, P. Montero, B. Mundim, P. Nelson, A. Nerozzi, S. C. Noble, C. Ott, L. J. Papenfort, R. Paruchuri, M. Pirog, D. Pollney, D. Price, D. Radice, T. Radke, C. Reisswig, L. Rezzolla, C. B. Richards, D. Rideout, M. Ripeanu, L. Sala, J. A. Schewtschenko, B. Schutz, E. Seidel, E. Seidel, J. Shalf, S. Shankar, K. Sible, U. Sperhake, N. Stergioulas, W.-M. Suen, B. Szilagyi, R. Takahashi, M. Thomas, J. Thornburg, C. Tian, W. Tichy, M. Tobias, A. Tonita, S. Tootle, P. Walker, M.-B. Wan, B. Wardell, H. Witek, M. Zilhão, B. Zink, and Y. Zlochower, *The Einstein Toolkit* (2024).
- [75] F. Loffler *et al.*, *Class. Quant. Grav.* **29**, 115001 (2012), arXiv:1111.3344 [gr-qc].
- [76] Canuda: Git Repository and Website (2023).
- [77] R. L. Arnowitt, S. Deser, and C. W. Misner, *Gen. Rel. Grav.* **40**, 1997 (2008), arXiv:gr-qc/0405109.
- [78] J. W. York, Jr., *Phys. Rev. Lett.* **28**, 1082 (1972).
- [79] J. W. York, Jr., in *Workshop on Sources of Gravitational Radiation* (1978) pp. 83–126.
- [80] O. Sarbach and M. Tiglio, *Living Rev. Rel.* **15**, 9 (2012), arXiv:1203.6443 [gr-qc].
- [81] M. Shibata and T. Nakamura, *Phys. Rev. D* **52**, 5428 (1995).
- [82] T. W. Baumgarte and S. L. Shapiro, *Phys. Rev. D* **59**, 024007 (1998), arXiv:gr-qc/9810065.
- [83] P. Marronetti, W. Tichy, B. Bruegmann, J. Gonzalez, and U. Sperhake, *Phys. Rev. D* **77**, 064010 (2008), arXiv:0709.2160 [gr-qc].
- [84] M. Campanelli, C. O. Lousto, P. Marronetti, and Y. Zlochower, *Phys. Rev. Lett.* **96**, 111101 (2006), arXiv:gr-qc/0511048.
- [85] J. G. Baker, J. Centrella, D.-I. Choi, M. Koppitz, and J. van Meter, *Phys. Rev. Lett.* **96**, 111102 (2006), arXiv:gr-qc/0511103.
- [86] M. Alcubierre, B. Bruegmann, P. Diener, M. Koppitz, D. Pollney, E. Seidel, and R. Takahashi, *Phys. Rev. D* **67**, 084023 (2003), arXiv:gr-qc/0206072.
- [87] J. R. van Meter, J. G. Baker, M. Koppitz, and D.-I. Choi, *Phys. Rev. D* **73**, 124011 (2006), arXiv:gr-qc/0605030.
- [88] M. Alcubierre, *Introduction to 3+ 1 numerical relativity*, Vol. 140 (Oxford University Press, 2008).
- [89] U. Sperhake, *Phys. Rev. D* **76**, 104015 (2007), arXiv:gr-qc/0606079.
- [90] T. W. Baumgarte and S. L. Shapiro, *Numerical Relativity: Solving Einstein's Equations on the Computer* (Cambridge University Press, 2010).
- [91] M. Shibata, *Numerical Relativity* (World Scientific Publishing Co., Inc., USA, 2015).
- [92] M. Zilhão, H. Witek, and V. Cardoso, *Class. Quant.*

- Grav.** **32**, 234003 (2015), arXiv:1505.00797 [gr-qc].
- [93] H. Okawa, H. Witek, and V. Cardoso, **Phys. Rev. D** **99**, 104032 (2014), arXiv:1401.1548 [gr-qc].
- [94] A. Lichnerowicz, **Bull. Soc. Math. Fr.** **72**, 146 (1944).
- [95] J. W. York, Jr., **Phys. Rev. Lett.** **26**, 1656 (1971).
- [96] J. Bamber, J. C. Aurrekoetxea, K. Clough, and P. G. Ferreira, **Phys. Rev. D** **107**, 024035 (2023), arXiv:2210.09254 [gr-qc].
- [97] J. M. Bowen and J. W. York, Jr., **Phys. Rev. D** **21**, 2047 (1980).
- [98] S. Dain, C. O. Lousto, and Y. Zlochower, **Phys. Rev. D** **78**, 024039 (2008), arXiv:0803.0351 [gr-qc].
- [99] G. Lovelace, R. Owen, H. P. Pfeiffer, and T. Chu, **Phys. Rev. D** **78**, 084017 (2008), arXiv:0805.4192 [gr-qc].
- [100] W. E. East, F. M. Ramazanoglu, and F. Pretorius, **Phys. Rev. D** **86**, 104053 (2012), arXiv:1208.3473 [gr-qc].
- [101] Y. Choquet-Bruhat, J. Isenberg, and J. W. York, Jr., **Phys. Rev. D** **61**, 084034 (2000), arXiv:gr-qc/9906095.
- [102] E. Gourgoulhon, 3+1 formalism and bases of numerical relativity (2007), arXiv:gr-qc/0703035.
- [103] H. Witek, M. Zilhao, G. Bozzola, C.-H. Cheng, A. Dima, M. Elley, G. Ficarra, T. Ikeda, R. Luna, C. Richards, N. Sanchis-Gual, and H. Silva, **Canuda: a public numerical relativity library to probe fundamental physics** (2023).
- [104] T. Goodale, G. Allen, G. Lanfermann, J. Massó, T. Radke, E. Seidel, and J. Shalf, in *Vector and Parallel Processing – VECPAR’2002, 5th International Conference, Lecture Notes in Computer Science* (Springer, Berlin, 2003).
- [105] Cactus developers, **Cactus Computational Toolkit**.
- [106] E. Schnetter, S. H. Hawley, and I. Hawke, **Class. Quant. Grav.** **21**, 1465 (2004), arXiv:gr-qc/0310042.
- [107] Carpet, Carpet: Adaptive Mesh Refinement for the Cactus Framework.
- [108] P. V. P. Cunha, J. A. Font, C. Herdeiro, E. Radu, N. Sanchis-Gual, and M. Zilhão, **Phys. Rev. D** **96**, 104040 (2017), arXiv:1709.06118 [gr-qc].
- [109] M. Ansorg, B. Bruegmann, and W. Tichy, **Phys. Rev. D** **70**, 064011 (2004), arXiv:gr-qc/0404056.
- [110] S. Habib, A. Ramos-Buades, E. A. Huerta, S. Husa, R. Haas, and Z. Etienne, **Class. Quant. Grav.** **38**, 125007 (2021), arXiv:2011.08878 [gr-qc].
- [111] NRPy+'s webpage, <http://nrpyplus.net/>.
- [112] O. Dreyer, B. Krishnan, D. Shoemaker, and E. Schnetter, **Phys. Rev. D** **67**, 024018 (2003), arXiv:gr-qc/0206008.
- [113] J. Thornburg, **Class. Quant. Grav.** **21**, 743 (2004), arXiv:gr-qc/0306056.
- [114] A. Ramos-Buades, S. Husa, and G. Pratten, **Phys. Rev. D** **99**, 023003 (2019), arXiv:1810.00036 [gr-qc].
- [115] S. Husa, M. Hannam, J. A. Gonzalez, U. Sperhake, and B. Bruegmann, **Phys. Rev. D** **77**, 044037 (2008), arXiv:0706.0904 [gr-qc].
- [116] J. Healy, C. O. Lousto, H. Nakano, and Y. Zlochower, **Class. Quant. Grav.** **34**, 145011 (2017), arXiv:1702.00872 [gr-qc].
- [117] A. Ciolfella, J. Healy, C. O. Lousto, and H. Nakano, **Phys. Rev. D** **110**, 084031 (2024), arXiv:2406.11564 [gr-qc].
- [118] Canuda Youtube Channel, available at <https://www.youtube.com/@canudanumericalrelativity1634>.
- [119] S. Habib, M. A. Scheel, and S. A. Teukolsky, **Phys. Rev. D** **111**, 084059 (2025), arXiv:2410.05531 [gr-qc].
- [120] A. Ramos-Buades, M. van de Meent, H. P. Pfeiffer, H. R. Rüter, M. A. Scheel, M. Boyle, and L. E. Kidder, **Phys. Rev. D** **106**, 124040 (2022), arXiv:2209.03390 [gr-qc].
- [121] G. Ficarra and C. O. Lousto, **Phys. Rev. D** **111**, 044015 (2025), arXiv:2409.18728 [gr-qc].
- [122] M. A. Scheel *et al.*, The SXS Collaboration’s third catalog of binary black hole simulations (2025), arXiv:2505.13378 [gr-qc].
- [123] I. Ruchlin, J. Healy, C. O. Lousto, and Y. Zlochower, **Phys. Rev. D** **95**, 024033 (2017), arXiv:1410.8607 [gr-qc].
- [124] J. Huang, M. C. Johnson, L. Sagunski, M. Sakellariadou, and J. Zhang, **Phys. Rev. D** **99**, 063013 (2019), arXiv:1807.02133 [hep-ph].
- [125] N. Speeney, E. Berti, V. Cardoso, and A. Maselli, **Phys. Rev. D** **109**, 084068 (2024), arXiv:2401.00932 [gr-qc].
- [126] G. Ficarra and C. O. Lousto, **Phys. Rev. D** **110**, 084072 (2024), arXiv:2406.11985 [gr-qc].
- [127] Z. Wang, T. Helfer, D. Traykova, K. Clough, and E. Berti, **Phys. Rev. D** **110**, 024009 (2024), arXiv:2402.07977 [gr-qc].
- [128] C. Dyson, J. Redondo-Yuste, M. van de Meent, and V. Cardoso, **Phys. Rev. D** **109**, 104038 (2024), arXiv:2402.07981 [gr-qc].
- [129] S. Roy, R. Vicente, J. C. Aurrekoetxea, K. Clough, and P. G. Ferreira, Scalar fields around black hole binaries in LIGO-Virgo-KAGRA (2025), arXiv:2510.17967 [gr-qc].
- [130] R. Cayuso, P. Figueras, T. França, and L. Lehner, **Phys. Rev. Lett.** **131**, 111403 (2023), arXiv:2303.07246 [gr-qc].
- [131] L. Aresté Saló, D. D. Doneva, K. Clough, P. Figueras, and S. S. Yazadjiev, **Phys. Rev. D** **112**, 084022 (2025), arXiv:2507.13046 [gr-qc].
- [132] G. Lara *et al.*, Signatures from metastable oppositely-charged black hole binaries in scalar Gauss-Bonnet gravity (2025), arXiv:2505.14785 [gr-qc].
- [133] J. M. Martin-Garcia, xAct: Efficient tensor computer algebra for the wolfram language, xAct Package, (2002 – 2022).
- [134] D. Brizuela, J. M. Martin-Garcia, and G. A. Mena Marugan, **Gen. Rel. Grav.** **41**, 2415 (2009), arXiv:0807.0824 [gr-qc].
- [135] G. Bozzola, **The Journal of Open Source Software** **6**, 3099 (2021), arXiv:2104.06376 [gr-qc].
- [136] C. R. Harris, K. J. Millman, S. J. van der Walt, R. Gommers, P. Virtanen, D. Cournapeau, E. Wieser, J. Taylor, S. Berg, N. J. Smith, R. Kern, M. Picus, S. Hoyer, M. H. van Kerkwijk, M. Brett, A. Haldane, J. F. del Río, M. Wiebe, P. Peterson, P. Gérard-Marchant, K. Shepard, T. Reddy, W. Weckesser, H. Abbasi, C. Gohlke, and T. E. Oliphant, **Nature** **585**, 357 (2020).
- [137] J. D. Hunter, **Computing in Science & Engineering** **9**, 90 (2007).
- [138] P. Virtanen, R. Gommers, T. E. Oliphant, M. Haberland, T. Reddy, D. Cournapeau, E. Burovski, P. Peterson, W. Weckesser, J. Bright, S. J. van der Walt, M. Brett, J. Wilson, K. J. Millman, N. Mayorov, A. R. J. Nelson, E. Jones, R. Kern, E. Larson, C. J. Carey, İ. Polat, Y. Feng, E. W. Moore, J. VanderPlas, D. Laxalde, J. Perktold, R. Cimrman, I. Henriksen, E. A. Quintero, C. R. Harris, A. M. Archibald, A. H. Ribeiro, F. Pedregosa, P. van Mulbregt, and SciPy 1.0 Contributors, **Nature Methods** **17**, 261 (2020).
- [139] I. Ruchlin, Z. B. Etienne, and T. W. Baumgarte, **Phys.**

- Rev. D **97**, 064036 (2018), arXiv:1712.07658 [gr-qc].
- [140] H.-J. Yo, T. W. Baumgarte, and S. L. Shapiro, Phys. Rev. D **66**, 084026 (2002), arXiv:gr-qc/0209066.